國立交通大學

電機學院　電信學程

碩 士 論 文

DFT 式跳頻信號擷取器之反干擾性能分析

Anti-Jam Performance of DFT-Based Acquisition Schemes for Frequency-Hopped Signals

研 究 生：張祖瑞

指導教授：蘇育德　教授

中 華 民 國 九 十 六 年 一 月

DFT 式跳頻信號擷取器之反干擾性能分析
Anti-Jam Performance of DFT-Based Acquisition Schemes for Frequency-Hopped Signals

研 究 生：張祖瑞　　Student：Tsu-Juei Chang

指導教授：蘇育德　教授　　Advisor：Dr. Yu Ted Su

國 立 交 通 大 學

電機學院　電信學程

碩 士 論 文

A Thesis

Submitted to College of Electrical and Computer Engineering

National Chiao Tung University

in partial Fulfillment of the Requirements

for the Degree of

Master of Science

in

Communication Engineering

Jan. 2007

Hsinchu, Taiwan, Republic of China

中華民國九十六年一月

國　立　交　通　大　學

博碩士論文全文電子檔著作權授權書

（提供授權人裝訂於紙本論文書名頁之次頁用）

本授權書所授權之學位論文，為本人於國立交通大學＿＿＿＿＿＿系所＿＿＿＿＿＿組，　95　學年度第　一　學期取得碩士學位之論文。

論文題目：DFT 式跳頻信號擷取器之反干擾性能分析

指導教授：蘇育德 教授

■ 同意　□不同意

本人茲將本著作，以非專屬、無償授權國立交通大學與台灣聯合大學系統圖書館：基於推動讀者間「資源共享、互惠合作」之理念，與回饋社會與學術研究之目的，國立交通大學及台灣聯合大學系統圖書館得不限地域、時間與次數，以紙本、光碟或數位化等各種方法收錄、重製與利用；於著作權法合理使用範圍內，讀者得進行線上檢索、閱覽、下載或列印。

論文全文上載網路公開之範圍及時間：	
本校及台灣聯合大學系統區域網路	■ 中華民國　年　月　日公開
校外網際網路	■ 中華民國　年　月　日公開

授 權 人：張祖瑞

親筆簽名：＿＿＿＿＿＿＿＿＿＿＿＿

中華民國　　年　　月　　日

國　立　交　通　大　學

博碩士紙本論文著作權授權書

（提供授權人裝訂於全文電子檔授權書之次頁用）

本授權書所授權之學位論文，為本人於國立交通大學_____系所_____組，95 學年度第 一 學期取得碩士學位之論文。

論文題目：DFT 式跳頻信號擷取器之反干擾性能分析

指導教授： 蘇育德 教授

■ 同意

本人茲將本著作，以非專屬、無償授權國立交通大學，基於推動讀者間「資源共享、互惠合作」之理念，與回饋社會與學術研究之目的，國立交通大學圖書館得以紙本收錄、重製與利用；於著作權法合理使用範圍內，讀者得進行閱覽或列印。

本論文為本人向經濟部智慧局申請專利(未申請者本條款請不予理會)的附件之一，申請文號為：_____，請將論文延至____年____月____日再公開。

授 權 人：張祖瑞

親筆簽名：_____

中華民國　　年　　月　　日

中 華 民 國　　年　　月　　日

D F T 式 跳 頻 信 號 擷 取 器 之 反 干 擾 性 能 分 析

學生：張祖瑞　　指導教授：蘇育德 教授

國 立 交 通 大 學　　電 機 學 院　　電 信 學 程 碩 士 班

摘　　要

隨著我們進入資訊時代，通訊安全的重要性更勝以往。在數位化戰場上，軍事通訊系統正面對著電子戰的威脅，其中通訊干擾便是最常見的電子戰威脅之一。展頻通訊系統具有對抗蓄意干擾的抗干擾能力是眾所週知的。在本論文中，我們首先回顧衛星通訊及通道的一些基本知識，我們以一些例子說明在受到干擾的環境下 Ka 頻段的鏈路分析。接著我們提出三種 DFT 式跳頻信號擷取器架構，其擷取過程是在時域及頻域中同時進行，此架構能夠於一個跳頻序列週期內計算出所有的測試統計量（test statistics）。文中並分別推導此架構在理想的加成性高斯雜訊通道（即雜訊功率已知），非理想的加成性高斯雜訊通道（雜訊功率需經由估測而得），以及非理想的加成性高斯雜訊通道加上寬頻帶雜訊干擾及部分頻帶雜訊干擾下使用不同的信號擷取器架構所產生之偵測機率及誤警機率的數學表示式。此外，文中同時提出了一些方法使信號擷取器在蓄意干擾的環境下能夠估計雜訊功率並將其正規化（normalization）。我們採用 Debruijn 序列作為擬隨機（pseudo random）模式的產生序列，這是由於 Debruijn 序列是一個長度為 2 的冪次的序列，這一點使我們可以有效率地運用快速傅立葉轉換演算法完成計算。文中並以各擷取架構之平均擷取時間相互比較。最後，對於此架構在前述不同場景下，提供了數值模擬結果。此外我們亦分別提供了使用一個週期較長及另一個週期較短的跳頻模式在理想的加成性高斯雜訊通道下的數值模擬結果。

Anti-Jam Performance of DFT-Based Acquisition Schemes for Frequency-Hopped Signals

student：Tsu-Juei Chang　　Advisors：Dr. Yu Ted Su

Degree Program of Electrical and Computer Engineering
National Chiao Tung University

ABSTRACT

As we are entering the information age, the communication security has become a more important issue than ever. Military communication systems are faced with the electronic warfare (EW) threat in the digitized battlefield. Communication jamming is one of the most-encountered EW threat. It is well known that the spread spectrum communications have the anti-jam capability against intentional jamming. In this thesis, we first review some basics of the satellite communications. Examples for Ka band link budget analysis in the adverse environment are given. We propose three different DFT-based discrete acquisition schemes for the acquisition of the frequency-hopped signals. The acquisition process proceeds in both time and frequency domain. The proposed schemes make acquisition in just one period become possible. Mathematical expressions for the detection probability and false alarm probability using various acquisition schemes in the ideal AWGN channel (noise power perfectly known), the non-ideal AWGN channel(noise power is estimated), the non-ideal AWGN channel with broad-band noise jamming and partial-band noise jamming are derived. We also propose methods for the estimation and normalization of the noise and the noise-plus-jamming power in the jamming environment. The Debruijn sequence is adopted as the pseudo random hopping pattern generating sequence since it has a code length of power of 2. This allows an efficient computation for FFT algorithm. Finally, numerical results of the system performance for the aforementioned scenarios are presented. Besides, we also give numerical results using hopping patterns with a longer and a shorter period.

Acknowledgement

I want to express my deepest gratitude to my advisor, Professor Yu Ted Su (蘇育德 教授), for his clear guidance and constant encouragement. The research can not be finished without his advice. I am also very thankful to the senior member, Yan-Xiu Zheng (鄭延修), in the Transmission and Networking (TNT) Laboratory, Department of Communication Engineering, National Chiao Tung University, for his patience and valuable opinions. I want to appreciate the Chief of my unit, Shi-Huei Yang (楊錫輝), who has been very supportive during my study of the master program. Special thanks go to Dr. Jung-Hong Deng (鄧俊宏 博士). Dr. Deng is with the Chung-Shan Institute of Science and Technology, who has helped me a lot in computer simulation. Thank Professor Po-Chiang Lu (呂伯強 教授) of Ching Yun University, who has always been a mentor when I felt trapped in my career. I also want to show my gratitude to Cheng-Chung Kaung (高正中), who has helped me in my research. Thank Professor Chung Chin Lu (呂忠津 教授) of Department of Electrical Engineering, National Tsing Hua University, Professor Chong-Yung Chi (祁忠勇 教授) of Institute of Communication Engineering, National Tsing Hua University, and Professor Ta-Sung Lee (李大嵩 教授) of Department of Communication Engineering, National Chiao Tung University. Their valuable opinions have made this thesis more complete. Finally, thank my beloved wife. She has been very thoughtful and encouraging in our daily life. Thank my mother for raising me up with her great maternal love.

Contents

List of Tables

List of Figures

Chapter 1

Introduction

The electronic warfare (EW) has played a vital role in the digitized battlefield and its impact on tactical communications can not be overemphasized. Satellite communications have always been an important maneuver of command and control (C2) for the combat commander in military operation and therefore is a potential target of EW threat. One of the most effective electronic counter-measurements (ECM) to disable the satellite communications is through the use of communication jamming. Therefore, anti-jam (AJ) capability has become the most critical measurement and requirement of a military communication system. To combat jamming, the communicators must prevent the adversary jammer from acquiring the prior knowledge of the signal characteristics being used. The transmitter achieves this by introducing unpredictability or randomness in the transmitted waveforms that is known to the intended receiver but not to the jammer.

In general, AJ strategies are built upon the following technologies: 1) wideband transmission, 2) multiple antennas (i.e. antenna array), 3) robust modulation, and 4) forward error-correcting (FEC) codes. Spread spectrum (SS) techniques belong to the first category and frequency-hopping (FH) is generally considered as a more robust and efficient electronic counter counter-measurement (ECCM) scheme than the direct sequence spread spectrum (DSSS) waveform. In conjunction with FHSS waveform, one can use either differential phase shift keying (DPSK) or M-ary phase shift keying (MFSK) to enhance the system's AJ robustness, as these two modulation schemes can be incoherently detected and is thus immune to phase noise.

Frequency-hopping spread spectrum (FHSS) communication is a method that introduces the randomness to the transmitted waveform by changing the carrier frequency

pseudo-randomly. The transmitted signals are called "frequency-hopped" or "FH" signals. The set of frequency carriers used by the FH signal is called the "hopset" or "hopping pattern". This pattern is controlled by a binary sequence called pseudo random sequence or PN sequence. The unpredictability of the hopping pattern ensures the anti-jam (AJ) capability of the FH signal against a sophisticated jamming threat. Without the knowledge of the hopping pattern, a jammer always allocates its jamming power uniformly across the total spectral range used by the FH signal. To achieve a certain jamming-to-signal power ratio in each frequency channel, the total jamming power has to increase linearly with the number of the FH channels. Current technology permits the FH bandwidth in the order of GHz.

An FHSS receiver must synchronized with the received code sequence before it can start the communication. Any misalignment between the received sequence and the local replica causes the signal power to fall down in the output of the receiver, which, in turn, results in failure of synchronization. Synchronization of the receiver to the received sequence or code can be separated into two phases. The initial coarse synchronization is called **acquisition**. During acquisition the code phase of the locally-generated PN sequence is trying to align with the received PN sequence within a fraction of a chip interval. Once the coarse alignment is achieved, the initial search process stops and the fine synchronization called **tracking** begins. Tracking maintains the synchronization between the locally-generated code with the incoming signal.

In [7], an acquisition receiver employing noncoherent, noise-normalized, matched-filter correlation detection was proposed. The search correlation detector consists of a bank of N_s parallel select-the-largest symbol processors followed by a line of delay devices and adders. Each symbol processor consists of a bank N_h hop processors. Within a hop processor, the envelop-detected outputs were weighted by the inverse of the perfectly known noise power (including jamming power) in each hop prior to the subsequent linear combing. As N_h becomes large, the number of hop processors becomes impractical large for complexity consideration. In [8], a serial search frequency hopping acquisition system was proposed. The system searches for the correct code phase by correlating the incoming code sequence with the locally generated replica of the code sequence. If the uncertainty region contains N_u cells, in the worst case, it may take $N_u L T_h$ time units to

achieve acquisition, where L and T_h are the code period and hop interval, respectively. For large N_u and L, the mean time to acquire grows correspondingly.

In the thesis, we shall focus on the issue of FHSS signal acquisition. We propose several DFT-based code acquisition schemes which are equivalent to the conventional matched-filter acquisition approach. Only uplink is considered for the position of the satellite is stationary and is known to various adversaries. Downlink jamming is less efficient for the locations of earth receivers are much difficult to detect. Satellite link usually provides large transmission bandwidth which is a good candidate for spread spectrum communications. Chapter 2 briefly reviews the satellite communication basics and analyzes some typical Ka band link budgets for AWGN channels and partial band noise jammed channels. Chapter 3 delineates the discrete acquisition scheme based on DFT. We derive the detection and false alarm probabilities for three decision criteria. Computer simulation results are given to validate our analysis and to examine the performance trends. Since a threshold is often needed for an acquisition decision and the optimal threshold is a function of signal-to-noise ratio (SNR), we suggest a method to obtain a reliable SNR estimate. Chapter 4 investigates AJ performance of the proposed acquisition schemes in the presence of noise jamming. In particular, to estimate the total noise-plus-jamming power superimposed on the received signal, a power estimator is added to the original scheme in Chapter 3. Mathematical expressions for detection probability and false alarm probability under full-band and partial-band noise jamming are derived. Computer simulation results are given. Chapter 5 summarizes our main results.

Chapter 2

Communication Satellite Channel

2.1 Satellite Communication Basics

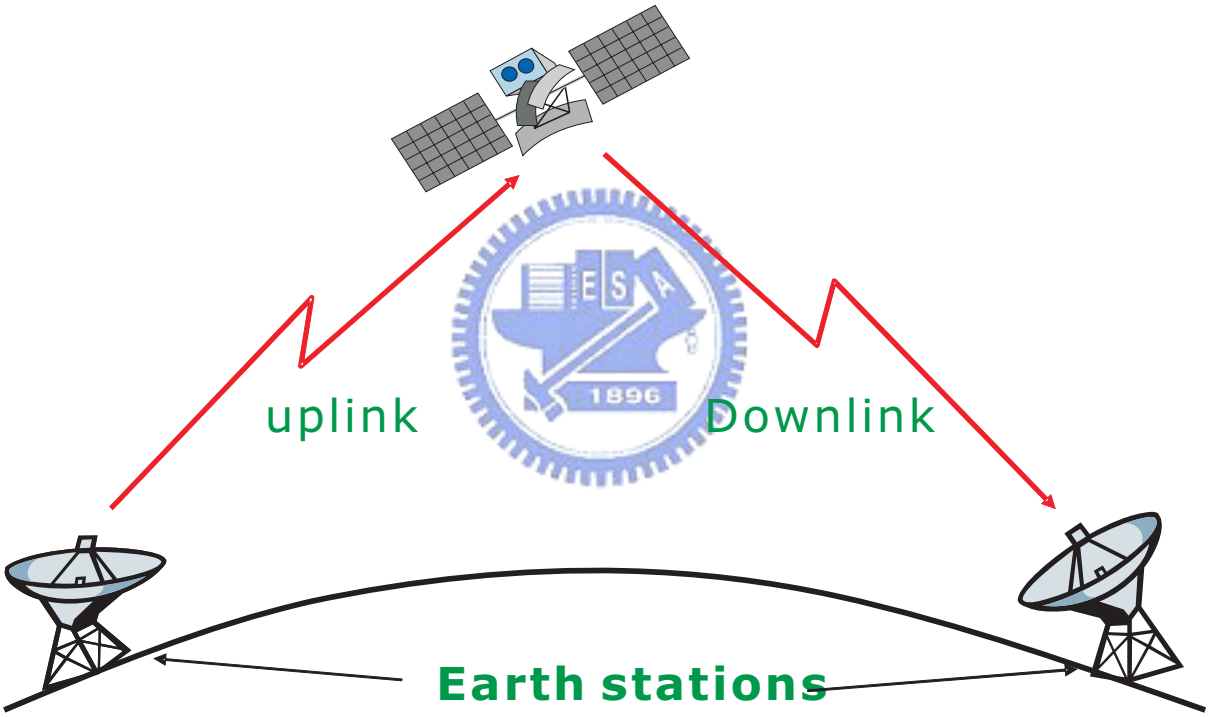

Figure 2.1: The components of a satellite communication system

A satellite communication system can be regarded as simply a amalgamation of basic communication systems which provides a type of long-range communication. Fig. 2.1 shows an *uplink* from an earth station to the satellite, and a *downlink* from the satellite back to the earth station. Radio wave is propagated via the uplink to the satellite. The satellite collects the impinging radio wave and retransmits the radio wave to some particular earth stations.

A satellite that merely passes on the uplink carrier to the downlink without additional signal processing function is named as a *relay satellite* or *repeater satellite*. A more common name is the *transponder*, since the satellite responds to the uplink and transmits the downlink.

An ideal active repeater satellite can be viewed as nothing but an electronic amplifier in orbit. Practical communication satellites involve a frequency translation from the uplink to the downlink to avoid the *ringaround* effect. The block diagram of a repeater satellite is sketched in Fig. 2.2. The uplink carrier is first received and filtered by the RF frontend . The filtered signal is then frequency-translated to another carrier used by the downlink. Finally, the downlink carrier is power-amplified for retransmission.

A satellite that collects the uplink carrier and performs some electronic processing-*on-board processing*-prior to retransmission is called a *processing satellite*. In a sophisticated processing satellite, the uplink carrier waveform is reconstructed on board, not merely frequency-translated, before it can be propagated down to the earth station. Fig. 2.3 depicts a satellite processing model with IF remodulation. The uplink carrier is frequency-translated to the IF, and the filtered IF carrier is "modulated" on to the downlink carrier. This system has the advantage that the uplink noise spectrum is not transferred directly to the downlink but is modulated onto the downlink carrier. The uplink noise is effectively concealed under the downlink carrier as a phase noise, which will not alter the required *Carrier-to-Noise Ratio* or *CNR* for establishing the receiver demodulation threshold.

Since a satellite's location in space has to be tracked it must be able to return the uplink *ranging waveform* for tracking purpose of the earth control station. Besides, for control purpose, satellites must be capable of receiving and decoding the command instructions from the earth control station. Fig. 2.4 shows the designated electromagnetic bands and

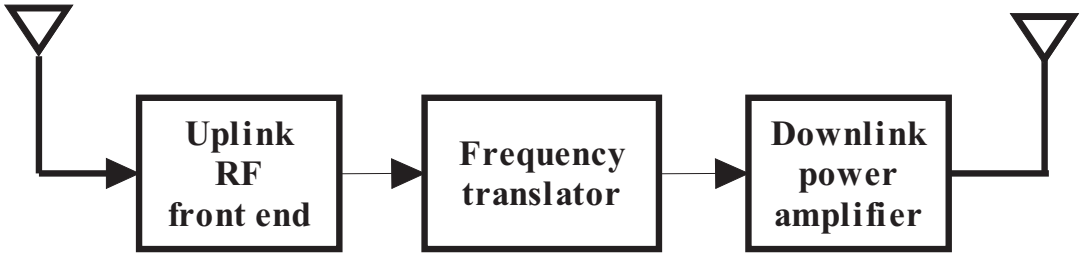

Figure 2.2: Block diagram for a repeater satellite.

some example services. The frequencies allocated for satellite communication are selected

from those bands that fulfill the requirements such as high power efficiency, minimal propagation loss and distortion, and low noise and interference effect. The operation frequencies used for satellite is regulated by the International Telecommunication Union (ITU).

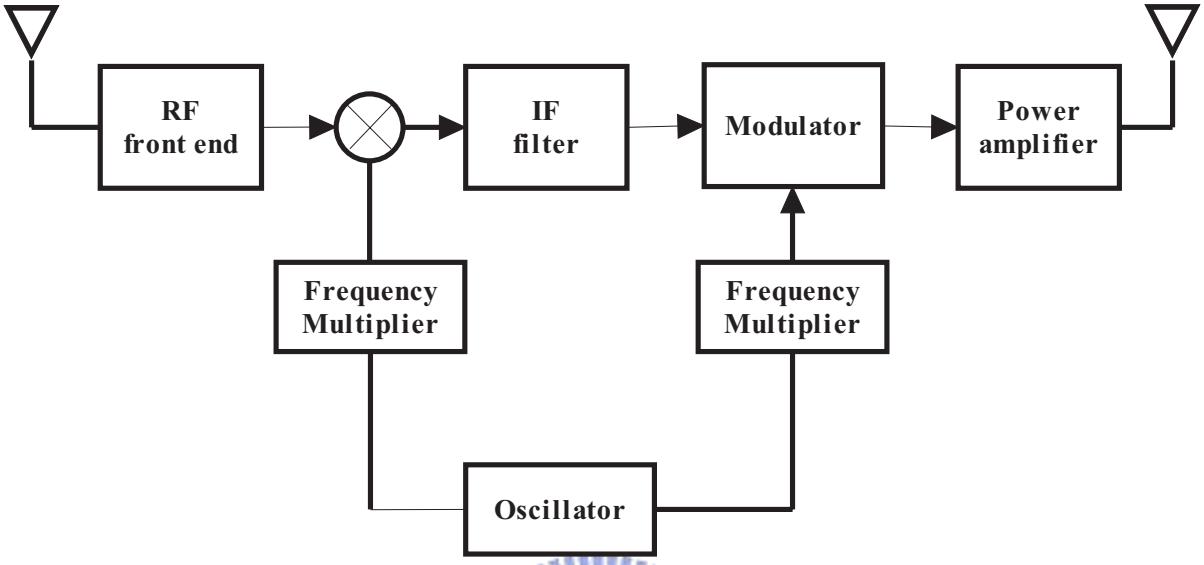

Figure 2.3: Block diagram for a processing satellite with IF remodulation.

Most of the satellite technologies developed in the early times was for the operation in UHF, C-band, and X-band. Recently, there is increased interest in extending the operation frequencies to higher frequency bands such as K-band and V-band. An obvious advantage of using the higher frequencies is the wider bandwidth available for transmission of information. More comprehensive and detailed discussions on satellite communications can be found in [1][2].

BANDS	FREQUENCY	EXAMPLE SERVICE
VHF	54 — 216 MHz	
UHF	470 — 890 MHz	Mobile satellite Services
L	0.39 — 1.55 GHz	Mobile Satellite Services, GPS
S	1.55 — 5.2 GHz	Deep-space research
C	3.9 — 6.2 GHz	Fixed,point-to-point,nonmilitary
X	5.2 — 10.9 GHz	Deep-space research, Military
K	10.9 — 36 GHz	
Ku	11.2 — 14.5 GHz	Broadcast,Fixed point,nonmilitary
Ka	17 — 31 GHz	Fixed,Mobile Satellite Service
Q	36 — 46 GHz	Fixed point,nonmilitary,Broadcast
V	46 — 56 GHz	Intersatellite

Figure 2.4: Designated communication satellite frequency bands.

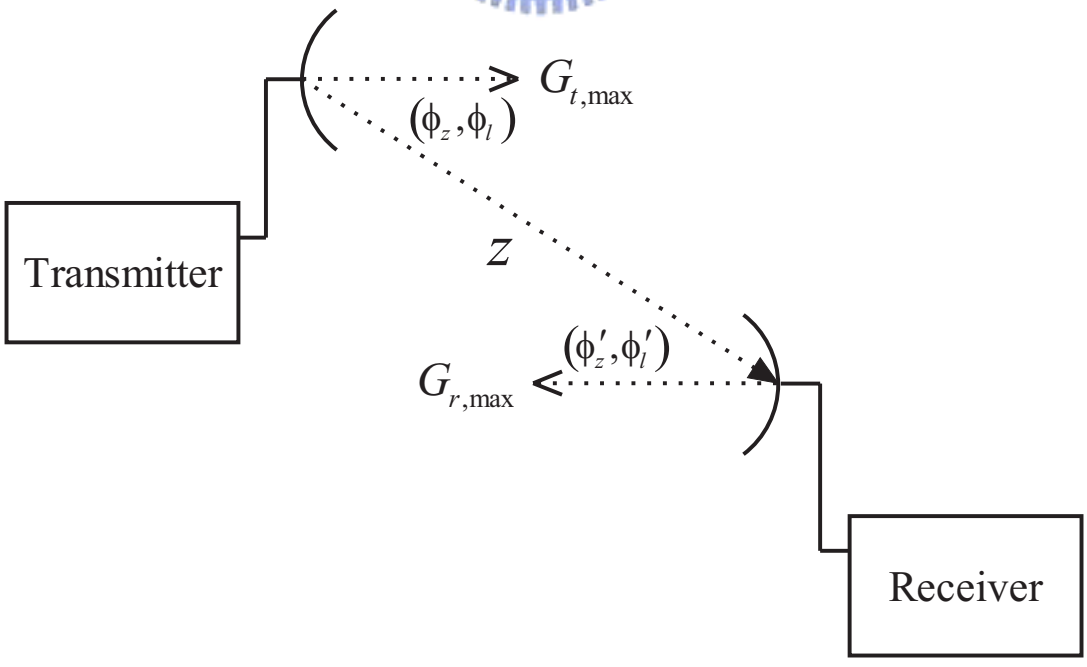

Figure 2.5: A point-to-point communication link.

2.2 Basic Satellite Link Analysis

The communication link between two points is established by the transmission of the carrier in the form of electromagnetic fields. The amount of received carrier power determines the capability of the receiver to demodulate or decode the information. Similar to the terrestrial microwave link, a satellite link is also a microwave link that uses the high-frequency band for transmission. The main difference, however, is that a satellite link transverses through the space, the atmosphere, where the radio wave may interact with rain drop, water vapor, fog, and gas particles. The earth station can also collect the galactic noise from the space. It is these impairments that make the satellite channel different from the terrestrial links.

2.2.1 Radio wave propagation and EIRP

Fig. 2.5 illustrates a typical point-to-point communication link. The transmitted RF power is characterized by its *effective isotropic radiated power (EIRP)*. The EIRP is defined by

$$EIRP = P_t G_t(\phi_z, \phi_l) \tag{2.1}$$

where P_t is the antenna input power from the transmitter power amplifier, and $G_t(\phi_z, \phi_l)$ is the gain in the direction (ϕ_z, ϕ_l) with respect to the direction of the maximum antenna gain of the transmitter. (ϕ_z, ϕ_l) denotes the azimuth and elevation angle respectively. The carrier power collected by the receiving antenna with an area A_r normal to the direction of the transmitter is characterized as

$$P_r = \frac{(EIRP)L_a}{4\pi z^2} A_r \tag{2.2}$$

where L_a accounts for the atmospheric losses during propagation and z is the propagation path length. Express the antenna area in terms of the receiving antenna gain in the direction of the transmitter

$$A_r = \left(\frac{\lambda^2}{4\pi}\right) G_r(\phi'_z, \phi'_l) \tag{2.3}$$

where λ is the carrier wavelength and $G_r(\phi'_z, \phi'_l)$ is the gain in the direction (ϕ'_z, ϕ'_l) with respect to the direction of the maximum gain of the receiving antenna. Substituting this result in (2.2) results in

$$P_r = (EIRP)L_a L_p G_r(\phi'_z, \phi'_l) \tag{2.4}$$

where

$$L_p = \left(\frac{\lambda}{4\pi z}\right)^2 \tag{2.5}$$

is the *propagation loss* of the link. Note that L_p is always present during propagation both in space and atmosphere. It is conventionally to express P_r in decibels

$$P_{r(dB)} = EIRP_{(dB)} + L_{p(dB)} + L_{a(dB)} + G_{r(dB)} \tag{2.6}$$

The *propagation loss*, L_p, can be converted to be frequency-dependent and has the value in decibel

$$L_{p(dB)} = -36.6 - 20log(z \cdot f) \tag{2.7}$$

where z is in miles and f in megahertz. An additional loss that should be included in L_a is the *polarization loss*. The *polarization loss* occurs when the polarization of the receiving antenna is not properly aligned with the polarization of the incoming wave.

2.2.2 Antenna gain

The transmitting antenna converts an electrical signal to electromagnetic field which can be radiated into the air. The receiving antenna collects the impinging electromagnetic field and converts it to an electrical signal.

The antenna gain pattern is the spatial distribution of the gain. The most important parameters of an antenna gain pattern includes its *gain* (the maximum values of its gain pattern), its *half-power beamwidth* (HPBW), and its *sidelobes*. The directional gain of the antenna directly determines the amount of the received carrier power. As an empirical rule, the maximum gain G_{max} and the HPBW ϕ_b in radians are given by

$$G_{max} = \eta_a\left(\frac{4\pi}{\lambda^2}\right)A \tag{2.8}$$

$$\phi_b \cong \frac{\lambda}{d\sqrt{\eta_a}} \tag{2.9}$$

where A is the antenna cross-sectional area, d is the diameter of that area, and η_a is the antenna efficiency factor. The most common type of antenna used in satellites and earth stations is the *parabolic reflector* or *dish*. For small angles off boresight, such that the skirts is within about 6dB of the peak value, the parabolic antenna pattern is sufficiently characterized by

$$G(\phi) \approx \eta_a\left(\frac{\pi d}{\lambda}\right)^2 e^{-2.76(\frac{\phi}{\phi_b})^2} \tag{2.10}$$

where ϕ denotes the small pointing error off the direction of G_{max}. In addition to the antenna efficiency loss, the roughness of the antenna dish also causes the scattering of radio wave. This roughness loss is accounted for by

$$L_r = e^{(\frac{-4\pi\sigma}{\lambda})^2} \tag{2.11}$$

where σ stands for the rms roughness in wavelength dimension. Note that as the frequency increases, L_r also increases, which degrades the increase in G_{max} in (2.8).

While G_{max} is the peak gain of the antenna, the actual gain involved in the power calculation depends on the relative angular direction from the transmitter to the receiver. The capability of accurate alignment between the satellite antenna and the earth station dish depends on the pointing and tracking capability of the system. The presence of the pointing error meas that the available gain in the skirts instead the peak gain of the receiver has to be used in the power calculation. For a parabolic reflector with pointing error ϕ_e, (2.10) shows that

$$G(\phi_e) = G_{max} \cdot e^{-2.76(\frac{\phi_e}{\phi_b})^2} \tag{2.12}$$

2.2.3 Atmospheric losses

A propagating wave is subject to the *propagation loss* L_p even in free space. When propagating through the atmosphere, it undergoes an additional power loss caused by absorption and scattering of the wave by the constituent particulates of the atmosphere. These particulates are a collection of gases, atoms, water droplets, pollutants, and so on captured by the Earth's gravity field. Since satellite links pass through the entire atmosphere, we don't consider the loss per kilometer of the link. The loss is a function of frequency and elevation angle. Lower elevation angle results in severer atmospheric loss because more of the path is within the atmosphere. When the frequency is increased to a point that the wavelength approaches the dimension of the particulates, the loss becomes significant. For example, severe absorption due to water vapor occurs at about 22 GHz and 180 GHz. Another severe absorption due to oxygen molecules occurs at about 60 GHz and 118 GHz.

2.2.4 Rain and fog attenuation

The power loss or attenuation due to rain and fog is more complicated than the *propagation loss* and *atmospheric loss* discussed. The attenuation is a function of the density

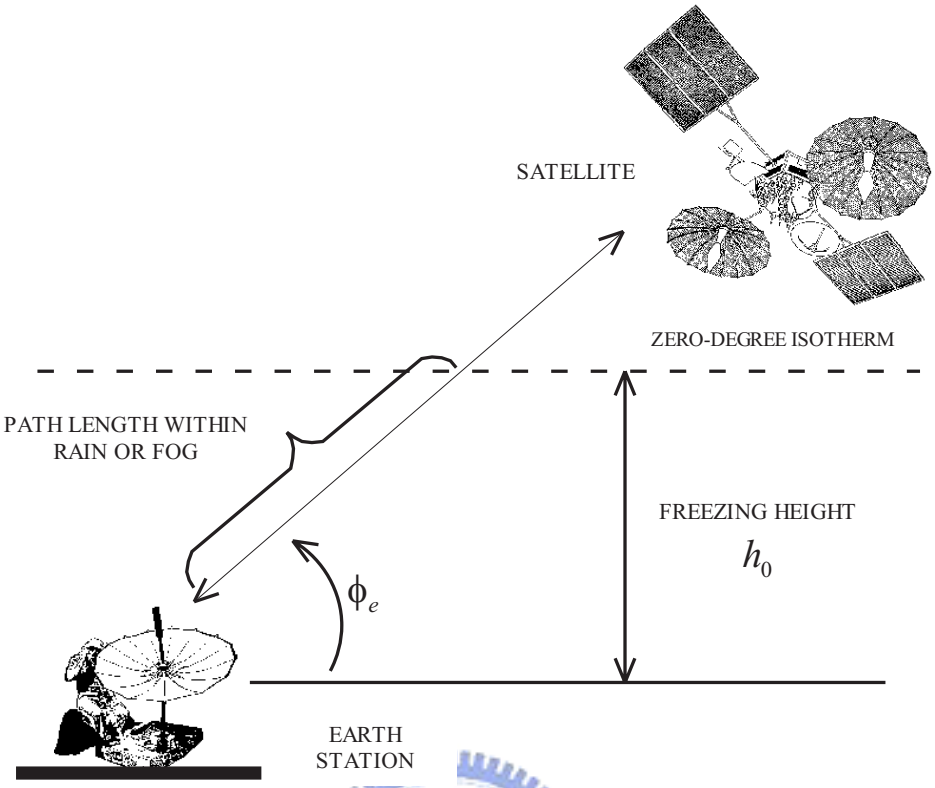

Figure 2.6: Rain or fog attenuation from the ground to the zero-degree isotherm.

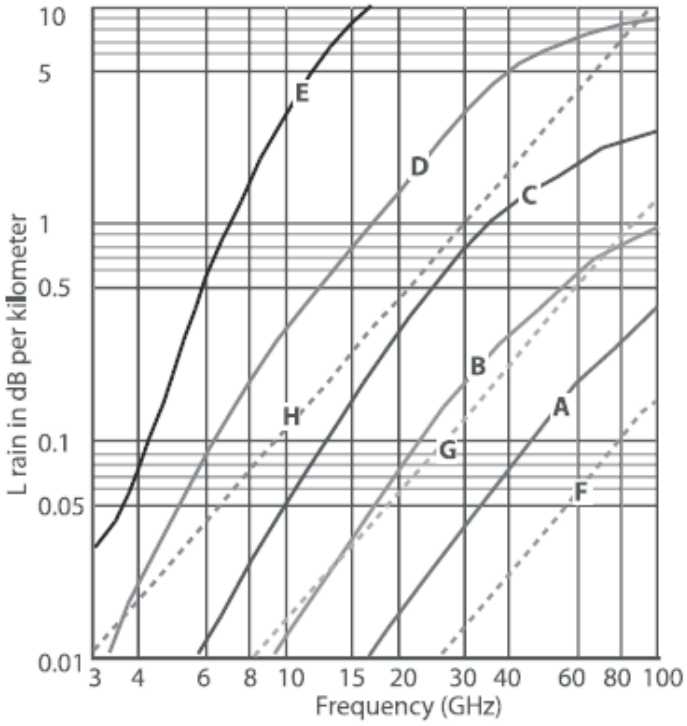

Figure 2.7: Rain and fog attenuation per kilometer v.s. the frequency

A	0.25 mm/hr	Drizzle
B	1.0 mm/hr	Ligth rain
C	4.0 mm/hr	Moderate rain
D	16 mm/hr	Heavy rain
E	100 mm/hr	Very heavy rain

F	0.032 gm/m^3	Visibility greater than 600m
G	0.32 gm/m^3	Visibility about 120m
H	2.3 gm/m^3	Visibility about 30m

Table 2.1: Rain and fog density for curves in Fig. 2.7

of the rain and fog, the path length within the rain and fog, and the frequency. Fig. 2.6 illustrates the geometry of the path length within the rain and fog. The freezing hight h_0 is the height from the ground to the zero-degree isotherm at which the water starts to become frozen. Above the isotherm, the droplets are ice instead of water. Ice droplets cause far less attenuation. According to Fig. 2.6, and [3], the path length within the rain and fog is computed as

$$l_r = \frac{h_0}{\sin \phi_e} \tag{2.13}$$

where h_0 denotes the freezing height, and ϕ_e the elevation angle of the earth station.

With the path length l_r at hand, we can determine the rain and fog attenuation by using Table 2.1 and Fig 2.7. First choose the proper curve in Fig. 2.7 according to the rain and fog density in Table 2.1. Next determine the attenuation in dB per kilometer corresponding to the operation frequency. Multiply the path length l_r by the attenuation per kilometer and one can obtain the total rain or fog attenuation in dB for that path length. For example, at the location 22° N latitude, for the probability of the occurrence of the freezing height being 0.01%, the freezing height, $h_0 = 5$ km. Let the elevation angle $\phi_e = 58°$, the path length within the rain or fog $l_r = 5\text{km}/\sin 58° \approx 5.9$ km. If the link is operating at 29.5 GHz and the moderate rain is present (use curve C), the attenuation is about 0.75 dB/km. The total power loss would be 0.75 dB/km × 5.9 km = 4.425 dB. It should be emphasized that this power loss is not a precise calculation but

a rough estimation.

2.2.5 Receiver noise

In addition to pick up the radio carrier from the satellite transmitter, the receiver of the earth station also collects interference or noise from other sources. This unwanted fields primarily originate from the background radiation of galactic and cosmic sources in the sky and atmospheric reradiation, and *radio frequency interference, (RFI)*, from terrestrial emitters.

In addition to these external noises, the internal electronics of the receiver can also generate thermal noise. These internal and external noise combined to define the total noise level of the receiving system. This noise level determines the required collected power level from the transmitter to make the subsequent signal processing possible.

The amount of the receiver noise level is represented by the *noise equivalent temperature*, T_{eq}°, which is defined as

$$T_{eq}^{\circ} = T_b^{\circ} + (NF - 1)290^{\circ} \tag{2.14}$$

where T_b° denotes the background noise from the galactic and cosmic noise and NF denotes the *noise figure* of the receiver. A noise source with a temperature T_{eq}° generates an effective one-sided noise spectral level of

$$N_{eq} = kT_{eq}^{\circ}\ W/Hz \tag{2.15}$$

where $k = 1.379 \times 10^{-23}\ W/KHz$ or $-228.6\ dBW/KHz$ is the *Boltzmann's constant*. The total noise power entering the receiver over a bandwidth Ω_{RF} is

$$P_n = kT_{eq}^{\circ}\Omega_{RF} \tag{2.16}$$

where Ω_{RF} is the RF bandwidth of the receiver. For example, let $T_b^{\circ} = 290K$, and $NF = 2.0\ dB$ or ≈ 1.585, the noise equivalent noise temperature $T_{eq}^{\circ} = 26.62\ dBK$ or $\approx 459.2\ K$, where K is the degree in Kelvin. If the RF bandwidth $\Omega_{RF} = 1$ GHz, from (2.16), the noise power can be computed as

$$P_n \approx 6.33 \times 10^{-6}\ \mu W \text{ or } \approx -112\ dB \tag{2.17}$$

2.2.6 Carrier-to-Noise Ratios

The RF carrier-to-noise ratio (CNR) is the ratio of the received carrier power to the total noise power of the receiver. In general, communication links require that $P_r \geq 10P_n$ for successful signal processing.

The CNR is defined as

$$CNR = \frac{P_r}{p_n} \tag{2.18}$$

where P_r and P_n are defined in (2.4) and (2.16), respectively. Substituting for P_r and P_n produces

$$CNR = \frac{(EIRP)L_pL_aG_r}{kT_{eq}^{\circ}\Omega_{RF}} \tag{2.19}$$

Normalizing the CNR by the RF bandwidth Ω_{RF}, we define the RF carrier-to-noise level ratio

$$\frac{C}{N_{eq}} = \frac{(EIRP)L_pL_aG_r}{kT_{eq}^{\circ}} \tag{2.20}$$

Rearranging (2.20) and we have

$$\frac{C}{N_{eq}} = \left[\frac{EIRP}{k}\right] \cdot [L_pL_a] \cdot \left[\frac{G_r}{T_{eq}^{\circ}}\right] \tag{2.21}$$

(2.21) separates the contributions from each subsystem to C/N_{eq}. The first bracket includes only the transmitter parameters, the second includes the propagation parameters, and the last the receiver parameters. Note that the receiver influences the C/N_{eq} through the ratio G_r/T_{eq}°. The CNR in decibel form is expressed as

$$CNR_{(dB)} = EIRP_{(dB)} - k_{(dB)} + L_{p(dB)} + L_{a(dB)} + \left(\frac{G_r}{T_{eq}^{\circ}}\right)_{(dB)} - \Omega_{RF(dB)} \tag{2.22}$$

2.3 Jamming Scenario

Fig. 2.8 illustrates the geometry of the communication jamming scenario in which the receiver is jammed. The jamming power arriving at the antenna of the receiver is

$$J = P_jG_{jr}G_{rj}L_{pj}L_{aj} \tag{2.23}$$

where P_j is the jammer output power, G_{jr} the transmitting antenna gain of the jammer in the direction of the receiver, G_{rj} the receiving antenna gain of the receiver toward the jammer, λ the wavelength, and L_{pj} and L_{aj} the jammer propagation loss and atmospheric loss, respectively.

For an earth-space communication uplink, (2.4) defines the carrier power arriving at the the receiver antenna. According to [3], to follow the conventional notation in electronic warfare or EW, we use the symbol S instead of P_r for the carrier power collected by the receiver antenna. The jamming-to-signal power ratio (JSR) can be expressed as

$$\frac{J}{S} = \frac{(EIRP_J)G_{rj}L_{pj}L_{aj}}{(EIRP)L_pL_aG_r} \tag{2.24}$$

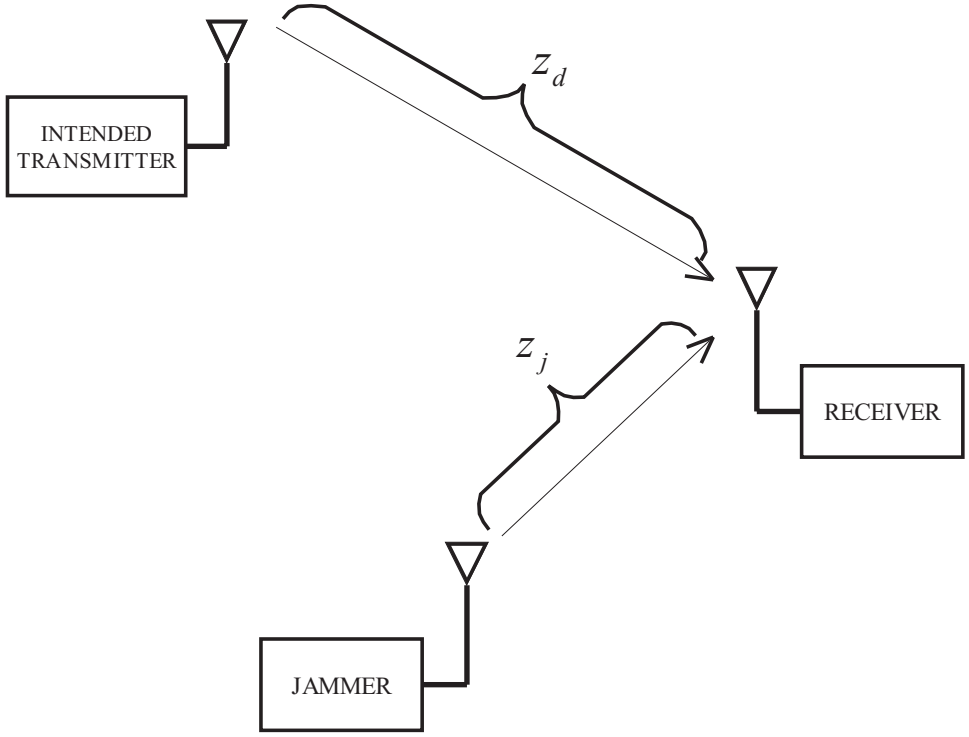

Figure 2.8: The communications jamming geometry.

where G_r is the receiver antenna gain in the direction of the intended transmitter. Suppose that $L_p = L_{pj}$ and $L_a = L_{aj}$ and express the JSR in decibels form, we have

$$JSR_{(dB)} = EIRP_{J(dB)} - (EIRP)_{(dB)} + G_{rj(dB)} - G_{r(dB)} \tag{2.25}$$

2.4 Ka Band Link Budget Analysis

In this section, we use the analysis results stated in the preceding section for the analysis of Ka band uplink budget. Different example scenarios under rain attenuation and the presence of jamming noise are given.

Consider the scenario illustrated in Fig. 2.9, the uplink jamming may or may not be present at the satellite receiver. The uplink analyses for various situations are given in table 2.2. Note that in the link budget analyses, the pointing error loss, the polarization loss, and the circuit loss (IFL loss) are also included in the calculation. For the jammer uplink, additional off-axis loss and circuit loss are considered. Since we assume that the uplink is an frequency hopping spread spectrum (FHSS) link, a processing gain presents in the calculation of the jamming-to-signal power ratio (JSR).

			Scenario					Remarks
	Entity parameters	unit	Clear Sky	Rain	Clear sky/Jam(1)	Rain/ Jam(1)	Rain/ Jam(2)	
	Earth Station							
1	**Frequency**	GHz	29.5	29.5	29.5	29.5	29.5	
2	**Antenna**							efficiency=60%
3	Elevation Angle	degree	58	58	58	58	58	
4	Diameter	m	0.6	0.6	0.6	0.6	0.6	
5	Directional gain	dBi	43.15	43.15	43.15	43.15	43.15	
6	Loss	dB	-3.9	-3.9	-3.9	-3.9	-3.9	estimated
7	**Transmitter power**	dB	3.01	13.98	3.01	9.03	13.98	
8		Watts	2	25	2	8	25	
9	**Earth station EIRP**	dBW	42.26	53.23	42.26	48.28	53.23	
10	**Boltzmann's constant**	dBW/K Hz	-228.6	-228.6	-228.6	-228.6	-228.6	
11	**Channel & Lossses**							z=36,332.72km
12	**Propagation loss**	dB	-213.12	-213.12	-213.12	-213.12	-213.12	assumed
13	**Atmospheric loss**	dB	NA	-20	NA	-20	-30	rain fade
14	**Pointing loss**	dB	-0.5	-0.5	-0.5	-0.5	-0.5	estimated
15	**Polarization loss**	dB	-0.2	-0.2	-0.2	-0.2	-0.2	estimated
16	**Satellite uplink receiver**							
17	**Antenna**							efficiency=60%
18	Diameter	m	2.54	2.54	2.54	2.54	2.54	
19	Directional gain	dBi	55.68	55.68	55.68	55.68	55.68	
20	Antenna temperature	K	290	290	290	290	290	
21	**Receiver noise figure**	dB	2	2	2	2	2	
22	**Sysytem temperature**	dBK	26.62	26.62	26.62	26.62	26.62	
23	**IFL loss**	dB	-3	-3	-3	-3	-3	
24	**G/T**	dB/K	26.06	26.06	26.06	26.06	26.06	
25	**Jammer**							
26	**Antenna**							efficienvy=60%
27	Diameter	m	5	5	5	5	5	
28	Directional gain	dBi	61.56	61.56	61.56	61.56	61.56	
29	IFL loss	dB	-2	-2	-2	-2	-2	
30	**Jammer transmitter**	dB	NA	NA	21.85	28.01	49.03	
31		Watts	0	0	153	632	80,000	
32	**Jammer EIRP**	dBW	59.56	59.56	81.41	87.57	108.59	
33	**Off-axis loss**	dB	-13	-13	-13	-13	-13	
34	**Pointing loss**	dB	-11	-11	-11	-11	-11	assumed
35	**Polarization loss**	dB	-0.2	-0.2	-0.2	-0.2	-0.2	
36	**Propagation loss**	dB	-213.12	-213.12	-213.12	-213.12	-213.12	
37	**Carrier bandwidth**	MHz	3.90625	3.90625	3.90625	3.90625	3.90625	
38	**Spread spectrum**	MHz	1,000	1,000	1,000	1,000	1,000	FHSS
39	**FH processing gain**	dB	24.08	24.08	24.08	24.08	24.08	
40	**SAT. received carrier**	dBW	-118.88	-127.91	-118.88	-132.86	-137.91	
41	**SAT. Carrier-to-noise power ratio (C/N)**	dB	17.18	8.15	17.18	3.20	-1.85	
42	**Jamming power at SAT. receiver**	dBW	NA	NA	-103.23	-117.07	-106.05	
43	**SAT.Jamming-to-signal power ratio**	dB	NA	NA	-8.43	-8.29	7.78	
44	**SAT. Carrier-to-noise level ratio (C/N_{eq})**	dBHz	83.10	74.07	83.10	69.12	64.07	

item 40=9+12+13+14+15+19+23
item 41=9-10+12+13+14+15+24-37
item 42=32+36+34+35+19+33+23
item 43=42-40-39

Table 2.2: Ka band Uplink analysis under different scenarios.

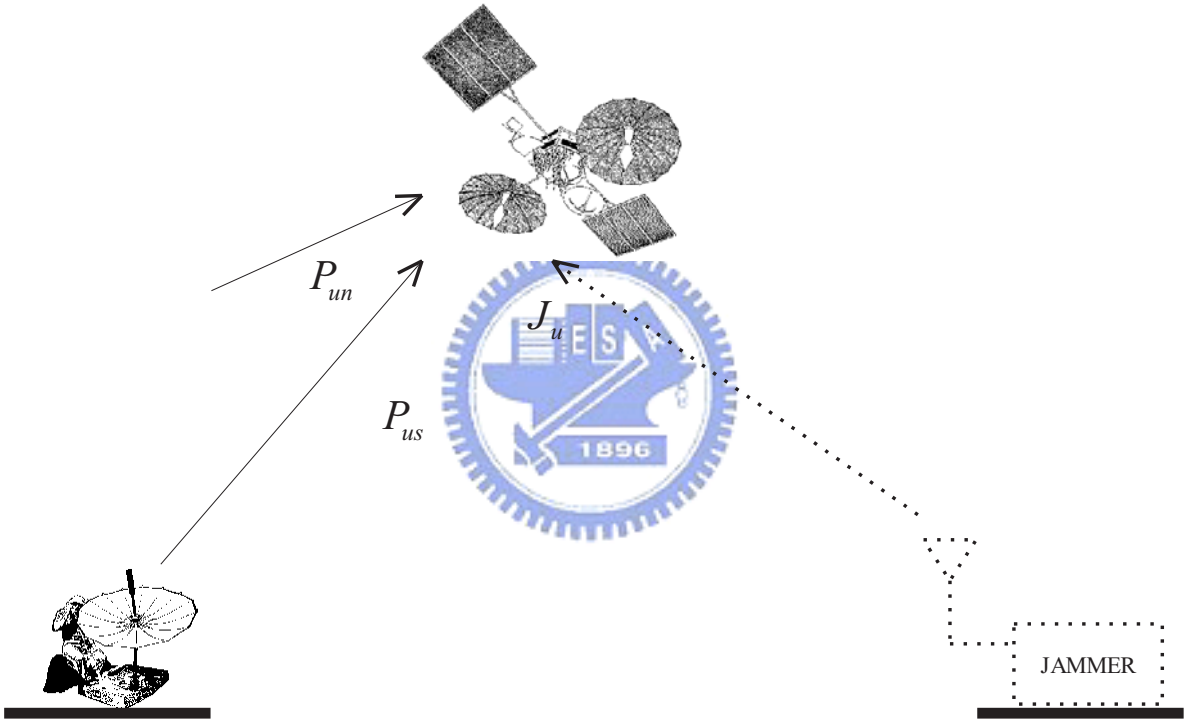

Figure 2.9: An uplink with or without jamming present.

Chapter 3

DFT-based frequency hopping code acquisition schemes

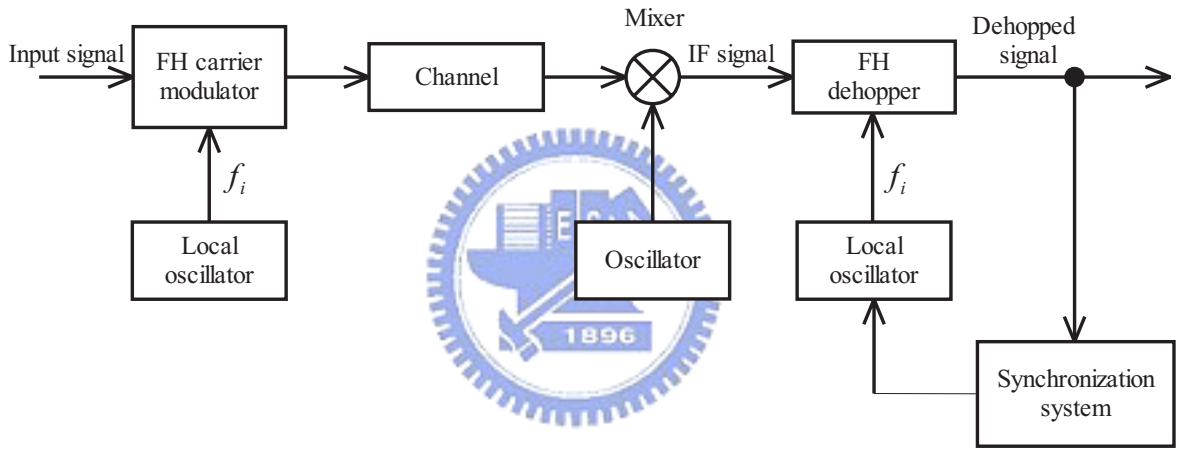

Figure 3.1: An frequency-hopping spread spectrum communication system.

Fig.3.1 illustrates the block diagram for an frequency-hopping spread spectrum communication system. The local oscillators at the transmitter and the receiver must generate the same frequency pattern. At the receiver, the synchronization system is responsible for the alignment of the locally generated FH sequence with the received one.

An frequency-hopped spread-spectrum (FHSS) receiver must generate a frequency hopping pattern (code) that is synchronized with the received FH pattern. That is, the corresponding FH chips or dwell intervals must precisely or nearly aligned. Unless FH synchronization is achieved, data demodulation and other post-detection processing can not proceed.

FH code synchronization process is often divided into two stages : The first stage is referred to as the (FH) code acquisition phase. It is a process that is responsible for

the alignment of the locally generated FH sequence with the received one such that the relative hop offset is less than half a hop interval. The purpose of the second stage is to further reduce the hop timing offset and maintain the offset to within a small number. Only the acquisition phase is considered in the thesis.

3.1 Matched-filter FH code acquisition scheme and its discrete equivalent

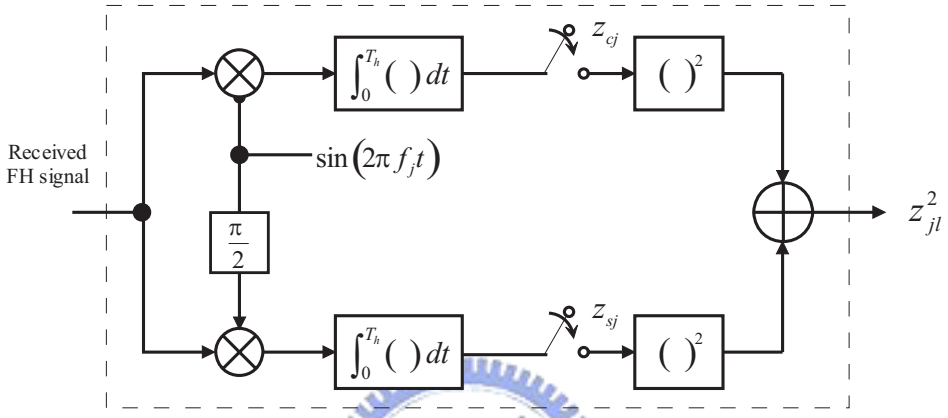

Figure 3.2: A single non-coherent demodulator.

For the receiver, there is an M-fold ambiguity associated with correct alignment of the FH sequence $b = \{b_1, b_2, \ldots, b_M\}$. The acquisition subsystem is responsible for resolve this ambiguity. An optimal (ML) synchronizer would use a bank of M matched filters with each one matched to one of the cyclic-shifted version of b, which results in the following possible patterns, $\{f_1, f_2, \cdots, f_M\}$, $\{f_2, f_3, \cdots, f_M, f_1\}, \{f_3, f_4, \cdots, f_M, f_1, f_2\}, \cdots, \{f_M, f_1, f_2, \cdots, f_{M-1}\}$. The corresponding complexity becomes impractical for large M. A feasible approach that solves the complexity issue is the serial search approach that uses a single matched filter (Fig.3.2) which examines each candidate FH pattern one-by-one. In the worst case, the serial search scheme might require M periods of the FH sequence before finding the correct one. A possible tradeoff is to use a combined parallel-serial search scheme that distributes the responsibility of resolving the M-fold ambiguity among L $(< M)$ matched filters. Fig. 3.3 illustrates a scheme using a bank of M non-coherent demodulators. Each non-coherent demodulator has two branches, each of which consists of a correlator, an integrate-and-dump device, and a square-law envelop detector. This non-coherent matched-filter bank performs analog short-term *Fourier Transform* of the incoming signal.

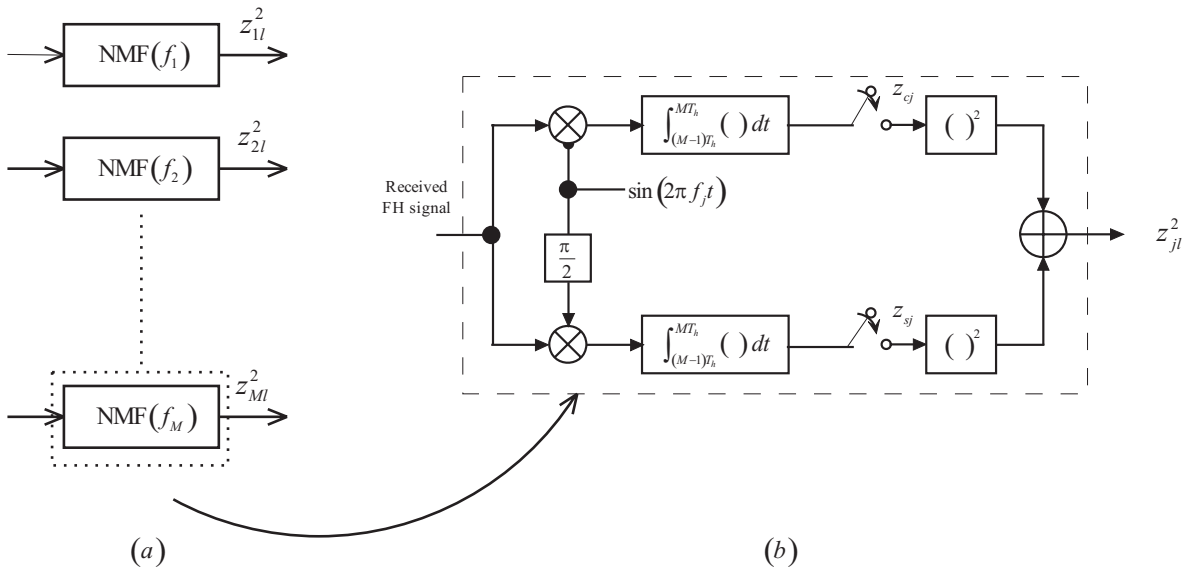

Figure 3.3: (a) A bank of non-coherent matched filters that performs DFT operation. (b) Non-coherent matched filter at $f = f_j$.

We shall derive the discrete equivalent of the matched-filter bank. Before starting the mathematical derivation, we make the following basic assumptions:

- No information modulation is involved during code acquisition.
- The misalignment between the received code sequence and the local code sequence is an integer multiple of one hop.
- Doppler shift induced by the transmission channel is negligible.
- The RF mixer has an idealistic rectangular frequency response.

The second assumption is illustrated in Fig. 3.4. With these assumptions on hand, we are ready to begin the derivation. In Fig. 3.3, the output of the j^{th} demodulator over $\big((l-1)T_h, lT_h\big]$ can be written as

$$\begin{aligned} |z_{jl}|^2 &= \Big(\int_{(l-1)T_h}^{lT_h} \tilde{r}(t)\cdot cos(2\pi f_j t)dt\Big)^2 + \Big(\int_{(l-1)T_h}^{lT_h} \tilde{r}(t)\cdot sin(2\pi f_j t)dt\Big)^2 \\ &= \Big|\,\mathscr{F}\{\tilde{r}(t)\}\,\Big|^2_{f=f_j} \text{ for } t \in \big((l-1)T_h, T_h\big] \end{aligned} \tag{3.1}$$

where $\mathscr{F}\{\bullet\}$ denotes the *Fourier Transform* operation and $\tilde{r}(t)$ is the down-converted FH signal. This result shows that the non-coherent matched-filter bank can be implemented by taking the DFT of the discrete version of the down-converted FH signal and then obtaining its squared magnitudes. A carrier selector and an FH pattern generater can also be added to complete the dehopping process. The frequency dehopper via DFT is shown in Fig. 3.5.

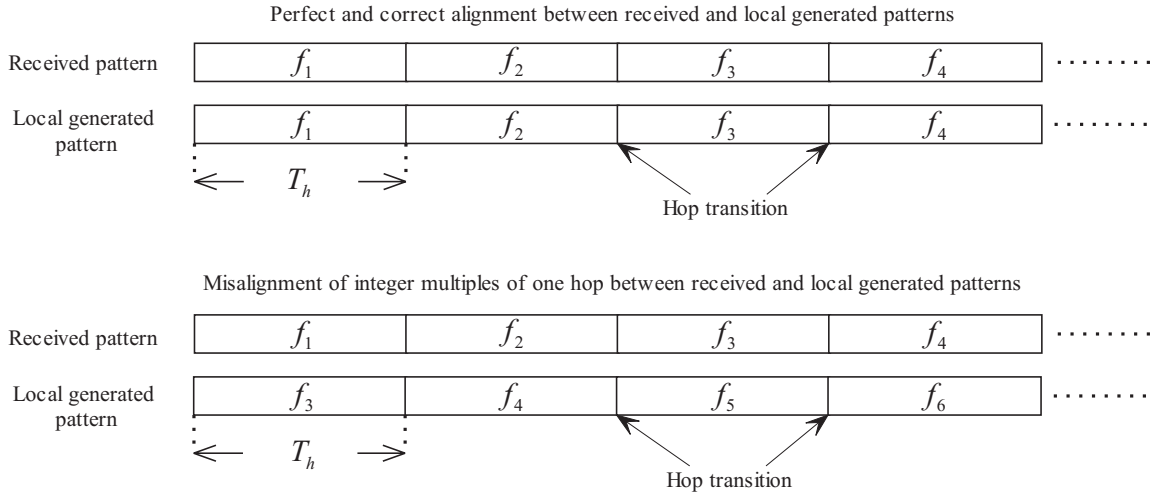

Figure 3.4: Two illustrative cases for hopping pattern alignment.

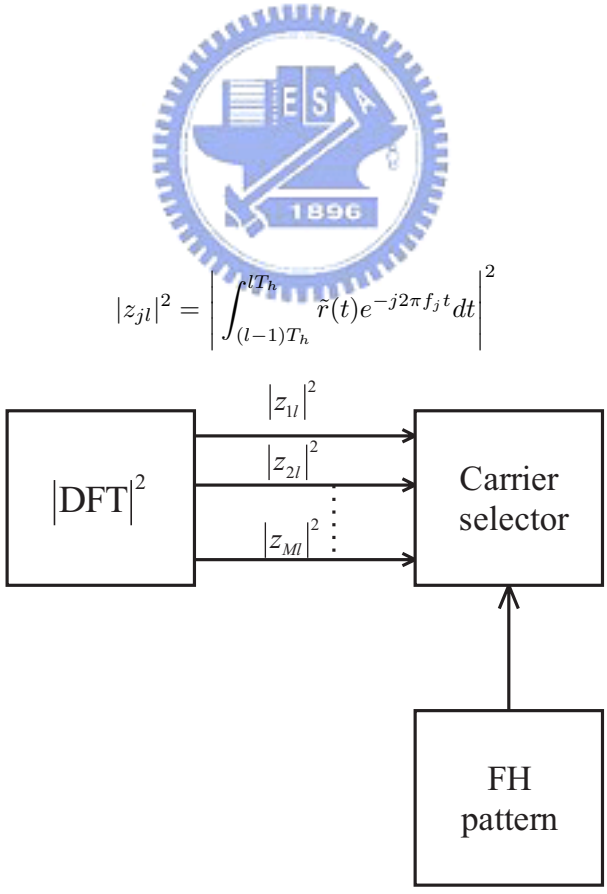

Figure 3.5: Frequency dehopper via DFT

3.2 Discrete equivalent code acquisition schemes

In this section, we propose various code acquisition schemes using the DFT-based structure.

3.2.1 An all-digital direct-conversion receiver architecture

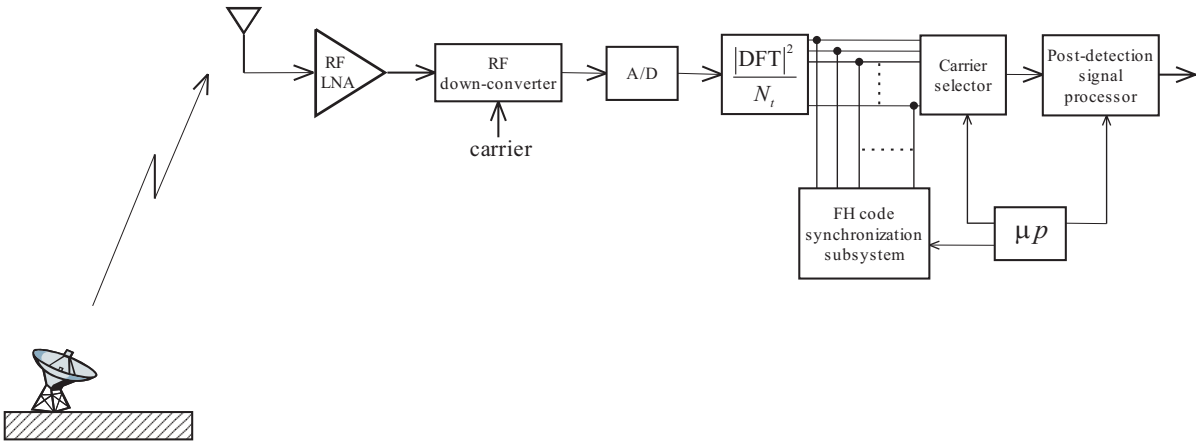

Figure 3.6: Direct-conversion all-digital programmable receiver.

Fig. 3.6 illustrates a direct-conversion all-digital programmable receiver. The receiver places a wide-band A/D converter at the output of the RF mixer and takes DFT on the output samples for further post-detection processing. The $|\mathrm{DFT}|^2$ is divided by N_t which is the FFT size so that the energy (or power) in the spectral domain is equal to that in the time domain [14]. Such a receiver architecture was used by an U.S. broadband satellite network in the early 90's. It is naturally suited for multi-carrier signals and allows very flexible signal processing options for anti-jam applications. For an FH waveform, the post-detection signal processor can then select the desired subchannel(s) for each DFT frame, immediately filtering all out-of-band noise and interference and fulfilling the frequency de-hopping process. Note that for the A/D, the sampling rate must be high enough to satisfy the Nyquist criterion to avoid aliasing.

As will be shown, efficient FH code acquisition schemes can be realized with this receiver architecture. In fact, a discrete parallel FH code acquisition scheme that accomplishes acquisition in just one period becomes possible. In other words, the FH code acquisition scheme can be implemented with an all-digital circuit. There is no need to use analog devices (except for the RF front end).

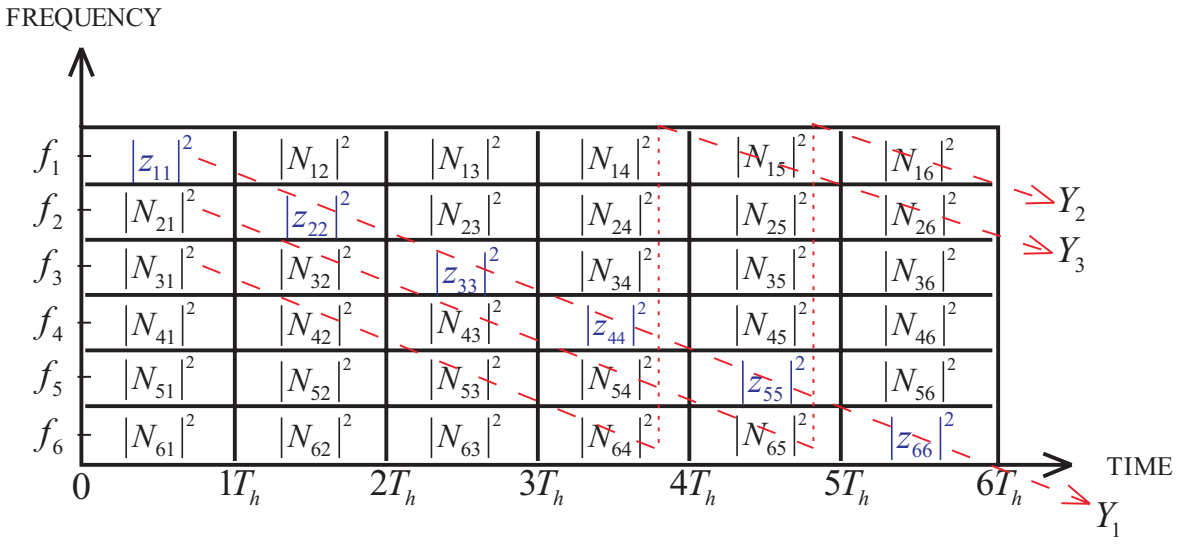

Figure 3.7: Time-frequency matrix of the acquisition process for the received frequency sequence $\{f_1, f_2, f_3, f_4, f_5, f_6\}$ (only 6 frequencies are shown for illustration).

3.2.2 Parallel computing of all possible test statistics

As mentioned before, there is M-fold ambiguity associated with correct alignment of the FH sequence. The DFT operation produces M squared spectral magnitude $|z_{jl}|^2$ of the down-converted FH signal in the l^{th} hop, each corresponding to f_j for $j = 1, 2, \cdots, M$. We define that $|z_{jl}|^2 = |S_{jl} + N_{jl}|^2$ when the signal is present, and $|z_{jl}|^2 = |N_{jl}|^2$ when the signal is absent. S_{jl} and N_{jl} represent the signal component and the noise component at frequency f_j in the l^{th} hop, respectively.

Fig. 3.7 illustrates the acquisition process of the discrete code acquisition scheme for the received frequency sequence $\{f_1, f_2, f_3, f_4, f_5, f_6\}$. Since the DFT spans the discrete spectrum of the signal, M (M=6 in this example) squared spectral magnitudes produce in Fig 3.7 during each hop. At the end of the first hop ($0 < t \leq 1T_h$), the squared magnitude $|z_{11}|^2$ at f_1 contains both the signal and noise components while the others contains only noise components. Similarly, at the end of the second hop ($1T_h < t \leq 2T_h$), the squared magnitude $|z_{22}|^2$ at f_2 contains both the signal and noise components while the others contains only noise component. By the same way, one can easily guess the results for the others. The following sums or test statistics can be computed simultaneously: (see the

dashed line in Fig. 3.7)

$$
\begin{aligned}
Y_1 &= |z_{11}|^2 + |z_{22}|^2 + |z_{33}|^2 + |z_{44}|^2 + |z_{55}|^2 + |z_{66}|^2 \\
&\quad \text{corresponding to } \{f_1, f_2, f_3, f_4, f_5, f_6\} \\
Y_2 &= |N_{21}|^2 + \cdots + |N_{16}|^2 \\
&\quad \text{corresponding to } \{f_2, f_3, f_4, f_5, f_6, f_1\} \\
Y_3 &= \cdots\cdots \\
&\quad \text{corresponding to } \{f_3, f_4, f_5, f_6, f_1, f_2\} \\
Y_4 &= \cdots\cdots \\
&\quad \text{corresponding to } \{f_4, f_5, f_6, f_1, f_2, f_3\} \\
Y_5 &= \cdots\cdots \\
&\quad \text{corresponding to } \{f_5, f_6, f_1, f_2, f_3, f_4\} \\
Y_6 &= |N_{61}|^2 + \cdots + |N_{56}|^2 \\
&\quad \text{corresponding to } \{f_6, f_1, f_2, f_3, f_4, f_5\}
\end{aligned}
$$

Let's consider one more case in which the frequency sequence $\{f_5, f_6, f_1, f_2, f_3, f_4\}$ is the correct FH pattern. The time-frequency matrix for this pattern is shown in Fig. 3.8. This time, the signal stays at f_5 during the first hop, then it hops to f_6 during the second hop, so on and so forth. The adder calculates the following sums: (see Fig. 3.8)

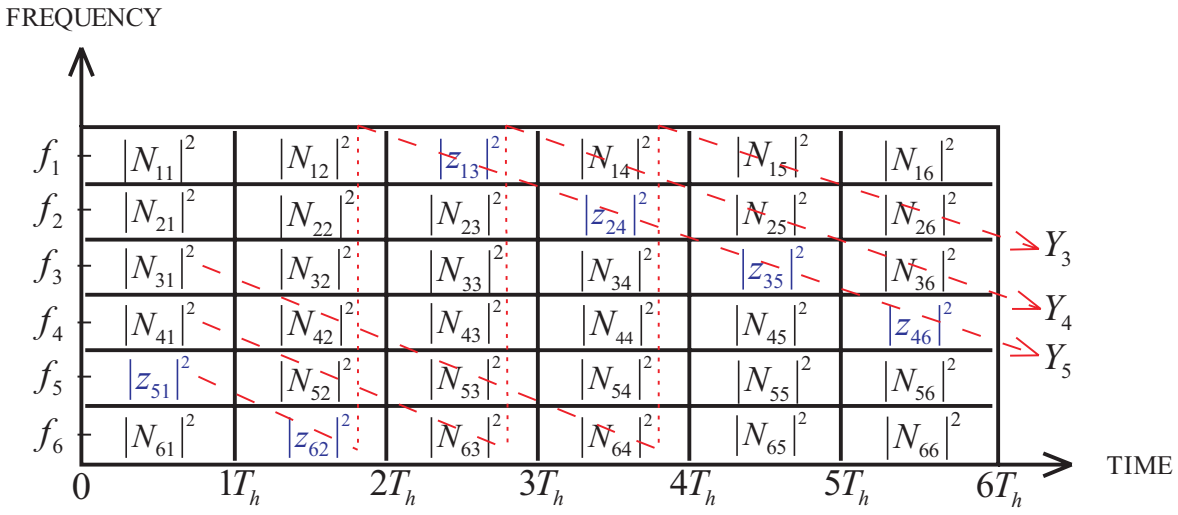

Figure 3.8: Time-frequency matrix of the acquisition process for the received frequency sequence $\{f_5, f_6, f_1, f_2, f_3, f_4\}$.

$$
\begin{aligned}
Y_1 &= |N_{11}|^2 + \cdots + |N_{66}|^2 \\
&\quad \text{corresponding to } \{f_1, f_2, f_3, f_4, f_5, f_6\} \\
Y_2 &= \cdots\cdots \\
&\quad \text{corresponding to } \{f_2, f_3, f_4, f_5, f_6, f_1\} \\
Y_3 &= \cdots\cdots \\
&\quad \text{corresponding to } \{f_3, f_4, f_5, f_6, f_1, f_2\} \\
Y_4 &= \cdots\cdots \\
&\quad \text{corresponding to } \{f_4, f_5, f_6, f_1, f_2, f_3\} \\
Y_5 &= |z_{51}|^2 + |z_{62}|^2 + |z_{13}|^2 + |z_{24}|^2 + |z_{35}|^2 + |z_{46}|^2 \\
&\quad \text{corresponding to } \{f_5, f_6, f_1, f_2, f_3, f_4\} \\
Y_6 &= |N_{61}|^2 + \cdots + |N_{56}|^2 \\
&\quad \text{corresponding to } \{f_6, f_1, f_2, f_3, f_4, f_5\}
\end{aligned}
$$

One can extends these results directly to the case in which M (> 6) frequencies $\{f_1, f_2, \cdots, f_M\}$ are used. After all the M sums have been calculated, all possible statistics are obtained. There are several advantage of the DFT-based scheme over the corresponding matched-filter bank:

1. The discrete code acquisition scheme can be implemented all with digital circuits. There is no need to use analog devices like the $\frac{\pi}{2}$ phase shifter, the mixer, and the integrator.

2. The discrete code acquisition scheme can achieve code acquisition in one period of the code sequence.

3. The spectral outputs from the DFT block can be fed to the channel state estimator (which will be included and explained later) to provide the channel state information.

3.2.3 ROC of the non-Coherent matched-filter bank

With all the possible statistics on hand, we are at a position to derive the mathematical expressions for the receiver operating characteristics (ROC) for the non-coherent matched filter.

The down-converted FH signal plus noise at the input to the demodulator bank can be expressed as

$$\tilde{r}(t) = \tilde{s}(t) + \tilde{n}(t) \tag{3.2}$$

for $(l-1T_h) \leq t < lT_h$. $l = 1, 2, \cdots, M$. The signal component can be written as

$$\tilde{s}(t) = A\cos(2\pi f_l t + \theta_l) + jA\sin(2\pi f_l t + \theta_l) \tag{3.3}$$

where A denotes the amplitude for both the in-phase and quadrature components, f_l the transmitted frequency for the l^{th} hop, and θ_l the initial signal phase associated with one particular hop. The phase θ_l is an independent random variable from hop to hop, and is uniformly distributed within the same hop. The noise can be written as

$$\tilde{n}(t) = n_c(t) + jn_s(t) \tag{3.4}$$

where $n_c(t)$, $n_s(t)$ are band-limited, independent, lowpass, zero-mean Gaussian noise processes with variance σ_0^2.

The output at a single non-coherent matched filter for the l^{th} hop is

$$z_{jl}^2 = (s_{jc} + n_c)^2 + (s_{js} + n_s)^2 \tag{3.5}$$

A sum variable or test statistics is formed by accumulating M "z_{jl}^2" each selected from one hop.

$$\begin{aligned} Y_1 &= z_{11}^2 + z_{22}^2 + \cdots + z_{MM}^2 \\ Y_2 &= z_{21}^2 + z_{32}^2 + \cdots + z_{M(M-1)}^2 \\ &\vdots \\ Y_M &= z_{1M}^2 + z_{12}^2 + \cdots + z_{(M-1)M}^2 \end{aligned} \tag{3.6}$$

Y_t for $t = 1, 2, \cdots, M$ each is a sum of the squares of 2M independent Gaussian random variables with common variance σ_0^2. M of these variables each has a mean of s_{jc} and another M each has a mean of s_{js} if the signal is present. All the 2M variables have a zero mean if the signal is not present. Let Y_i denotes the sum variable that contains all the FH signal components, that is, $s_{jc} = s_{js} = A$, and Y_i has a non-central chi-square *Probability Distribution Function (PDF)* given as [4]

$$f_Y(y_i \mid \text{signal present}) = \begin{cases} \frac{1}{2\sigma_0^2}\left(\frac{y_i}{s^2}\right)^{(M-1)/2} e^{-(s^2+y_i)/2\sigma_0^2} \cdot I_{M-1}(\sqrt{y_i}\frac{s}{\sigma_0^2}), & y_i \geq 0 \\ 0 & \text{o.w.} \end{cases} \tag{3.7}$$

where $s^2 = \sum_{j=1}^{M} A^2 = MA^2$ is the non-centrality factor and $I_n(\cdot)$ is the *modified Bessel function of the* 1^{st} *kind.*

For all the other sum variables $Y_t, t \neq i$, that contain only noise components, that is, $s_{jc} = s_{js} = 0$, each Y_t has a central chi-square *PDF* given as

$$f_Y(y_t \mid \text{signal absent}) = \begin{cases} \frac{1}{\sigma_0^{2M} 2^M \Gamma(M)} y_t^{(M-1)} e^{-y_t/2\sigma_0^2}, & y_t \geq 0 \\ \\ 0 & \text{o.w.} \end{cases} \tag{3.8}$$

where $\Gamma(\cdot)$ is the Gamma function.

The probability that Y_i exceeds the threshold η when the signal is present is

$$\begin{aligned} P_d &= \int_{\eta}^{\infty} f_Y(y_i|\text{signal present}) dy_i \\ &= 1 - \int_{0}^{\eta} f_Y(y_i|\text{signal present}) dy_i \\ &= 1 - \int_{0}^{\eta} \frac{1}{2\sigma_0^2} \Big(\frac{y_i}{s^2}\Big)^{(M-1)/2} e^{-(s^2+y_i)/2\sigma_0^2} \cdot I_{M-1}(\sqrt{y_i}\frac{s}{\sigma_0^2}) dy_i \\ &= 1 - F_Y(\eta|\text{signal present}) \end{aligned} \tag{3.9}$$

where $F_Y(\cdot)$ denotes the *Cumulative Distribution Function(CDF)* of Y.
For $m = \frac{1}{2}(2M) = M$ being an integer,

$$F_Y(\eta|\text{signal present}) = 1 - Q_M\big(\frac{s}{\sigma_0}, \frac{\sqrt{\eta}}{\sigma_0}\big) \tag{3.10}$$

and by using (3.10) in (3.9), we have

$$P_d = Q_M\big(\frac{s}{\sigma_0}, \frac{\sqrt{\eta}}{\sigma_0}\big) \tag{3.11}$$

In (3.11), $Q_m(a,b) = \int_b^{\infty} x\Big(\frac{x}{a}\Big)^{m-1} e^{-(x^2+a^2)/2} \cdot I_{m-1}(ax)dx$ is the *generalized Marcum's Q function of order* m .

The probability that a $Y_t, t \neq i$, exceeds η when the signal is absent is

$$\begin{aligned} P_{fa} &= \int_{\eta}^{\infty} f_Y(y_t|\text{signal absent}) dy_t \\ &= 1 - \int_{0}^{\eta} f_Y(y_t|\text{signal absent}) dy_t \\ &= 1 - \Big(\frac{1}{\sigma_0^{2M} 2^M \Gamma(M)}\Big) \int_{0}^{\eta} y_t^{(M-1)} e^{-y_t/2\sigma_0^2} dy_t \\ &= 1 - F_Y(\eta|\text{signal absent}) \end{aligned} \tag{3.12}$$

The *CDF* is computed as

$$F_Y(\eta|\text{signal absent}) = 1 - e^{-\eta/2\sigma_0^2} \sum_{j=0}^{M-1} \frac{1}{j!}\Big(\frac{\eta}{2\sigma_0^2}\Big)^j \tag{3.13}$$

and by using (3.13) in (3.12)

$$P_{fa} = e^{-\eta/2\sigma_0^2} \sum_{j=0}^{M-1} \frac{1}{j!}\Big(\frac{\eta}{2\sigma_0^2}\Big)^j \tag{3.14}$$

3.2.4 Serial acquisition scheme

The serial acquisition scheme compares each of the accumulated sum variables against a preset threshold η in a serial order. Once any one of the M sum variables being tested has a value greater than η, the test stops and a detection is declared. For example, if the j^{th} sum variable, Y_j, exceeds the threshold η, a declaration of "coarse synchronization achieved" is made and the frequency sequence $\{f_j, f_{j+1}, \cdots, f_{j-2}, f_{j-1}\}$ is recognized. If the signal is actually present and received in the declared pattern, an event of a correct detection occurs. However, if the signal is not present, an event of false alarm has occurred.

Let's assume that the threshold-test process begins from the first sum variable without loss of generality. A correct detection occurs if the i^{th} sum variable Y_i contains signal components and has a value greater than or equals η. According to the above statements, the probability of a correct detection, P_D, can be characterized as

$$\begin{aligned} P_D &= \frac{1}{M}\sum_{i=1}^{M}(1-P_{fa})^{i-1}P_d \\ &= \frac{P_d}{M}\cdot\frac{1-(1-P_{fa})^M}{P_{fa}} \end{aligned} \tag{3.15}$$

where P_d and P_{fa} are given in (3.11) and (3.14), respectively.

An false alarm occurs if any one of the sum variable Y_i that contains only noise components has a value greater than or equals η. (doesn't matter if the signal is present or absent). The false alarm probability is

$$P_{FA} = 1 - P_D - (1-P_{fa})^{M-1}(1-P_d) \tag{3.16}$$

The last term in (3.16) is the *miss probability* of the serial scheme, that is,

$$P_M = (1-P_{fa})^{M-1}(1-P_d) \tag{3.17}$$

3.2.5 Maximum likelihood acquisition scheme

In the maximum likelihood acquisition scheme, we select the maximum sum variable Y_j and recognize that the corresponding frequency sequence is the received sequence. In mathematical form, the probability of a correct detection is given by

$$\begin{aligned} P_D &= \text{Prob}\{y_j = max\ y_i; i = 1, 2, \cdots, M | \text{signal present}\} \\ &= \int_0^\infty f_Y(y_j|\text{signal present}) \left[\prod_{i=1, i\neq j}^{M} \int_0^{y_j} f_Y(y_i|\text{signal absent}) dy_i \right] dy_j \end{aligned} \quad (3.18)$$

When the signal is present, $f_Y(y_j|\text{signal present})$ is an non-central chi-square distribution; see (3.7). The operand of the consecutive product operator represents the CDF of each of the other M-1 sum variables with values smaller than y_j. $f_Y(y_i|\text{signal absent})$ is a central chi-square distribution. The CDF can be computed via (3.13).

Next, we shall use (3.7) in (3.18) for the derivation of an analytical expression for P_D. The following changes of the variables are needed.

$$s^2 = 2\sigma_0^2 M\hat{\beta} \quad (3.19)$$

$$y = 2\sigma_0^2 \hat{y} \quad (3.20)$$

Substituting (3.19) and (3.20) into (3.7), we obtain

$$f_{\hat{Y}}(\hat{y}|\text{signal present}) = \begin{cases} \frac{1}{2\sigma_0^2} \check{f}(\hat{y} \mid \text{signal present}), & \hat{y} \geq 0 \\ \\ 0 & \text{o.w.} \end{cases} \quad (3.21)$$

where

$$\check{f}(\hat{y} \mid \text{signal present}) = \frac{1}{2\sigma_0^2} \left(\frac{\hat{y}}{M\hat{\beta}} \right)^{(M-1)/2} e^{-(M\hat{\beta}+\hat{y})} \cdot I_{M-1}(2\sqrt{M\hat{\beta}\hat{y}}) \quad (3.22)$$

if the signal is present. Using (3.20) in (3.8) results in

$$f_{\hat{Y}}(\hat{y}|\text{signal absent}) = \begin{cases} \frac{1}{2\sigma_0^2} \check{f}(\hat{y} \mid \text{signal absent}), & \hat{y} \geq 0 \\ \\ 0 & \text{o.w.} \end{cases} \quad (3.23)$$

where

$$\check{f}(\hat{y} \mid \text{signal absent}) = \frac{\hat{y}^{(M-1)}}{\Gamma(M)} e^{-\hat{y}} \quad (3.24)$$

if the signal is absent.

For the clarity of notations, we use y in place of y_j and y_i since they actually represent the same random variable. Substitute (3.21) for $f(y_j|\text{signal present})$, (3.23) for $f(y_i|\text{signal absent})$ in (3.18) and the detection probability can be expressed as

$$\begin{aligned} P_D &= \int_0^\infty \check{f}(\hat{y} \mid \text{signal present}) \left[\int_0^{\hat{y}} \check{f}(\hat{y} \mid \text{signal absent}) d\hat{y} \right]^{(M-1)} d\hat{y} \\ &= \int_0^\infty \check{f}(\hat{y} \mid \text{signal present}) \left[\gamma(\hat{y}, M) \right]^{(M-1)} d\hat{y} \end{aligned} \tag{3.25}$$

where $\gamma(a, b)$ is the *Incomplete Gamma function*.

False alarm probability is the complement of P_D, and can be computed by

$$P_{FA} = 1 - P_D \tag{3.26}$$

From [5], for large M, (3.25) must be evaluated with alternate methods. Since the derivation is beyond the scope of our analysis, we will not present the derivation here.

3.2.6 Max-threshold acquisition scheme

In the serial acquisition scheme, each of the M sum variables is threshold-tested against a preset threshold η one by one. The acquisition process continues until a sum variable value is equal to or greater than η. While in the maximum likelihood acquisition scheme, the maximum sum variable is selected and the corresponding hopping pattern is considered as the correct pattern. A hybrid test that combines the features of these two schemes is possible. One decides that the correct hopping pattern is the one corresponding to the maximum sum variable which is greater than the preset threshold η. We refer to this scheme as the max-threshold acquisition scheme.

For the max-threshold acquisition scheme, the detection probability, P_D, is the probability that the maximum sum variable Y_j exceeds the threshold η when an FH signal is present. In mathematical form, it reads

$$\begin{aligned} P_D &= \text{Prob}\{y_j = (max\ y_i) \geq \eta; i = 1, 2, \cdots, M | \text{signal present}\} \\ &= \int_\eta^\infty f(y_j|\text{signal present}) \left[\prod_{i=1, i\neq j}^{M} \int_0^{y_j} f(y_i|\text{signal absent}) dy_i \right] dy_j \end{aligned} \tag{3.27}$$

This expression is identical to (3.18) except that the lower limit, 0, of the outer integration is replaced with the threshold η. Again, we replace the variable y by y_j and y_i. Substituting (3.21) and (3.23) into $f(y_j|\text{signal present})$ and $f(y_i|\text{signal absent})$ in (3.27)

and making a corresponding normalization of the integration limits, we obtain

$$\begin{aligned} P_D &= \int_{\hat{\eta}}^{\infty} \check{f}(\hat{y} \mid \text{signal present}) \left[\int_0^{\hat{y}} \check{f}(\hat{y} \mid \text{signal absent}) d\hat{y} \right]^{(M-1)} d\hat{y} \\ &= \int_{\hat{\eta}}^{\infty} \check{f}(\hat{y} \mid \text{signal present}) \left[\gamma(\hat{y}, M) \right]^{(M-1)} d\hat{y} \end{aligned} \tag{3.28}$$

On the other hand, the false alarm probability is

$$P_{FA} = 1 - \left[\prod_{i=1}^{M} \left(\int_0^{\eta} f_{\hat{Y}}(\hat{y}) d\hat{y} \right) \right] \tag{3.29}$$

Substituting (3.23) into (3.29) and replacing η by $\hat{\eta}$, we have

$$\begin{aligned} P_{FA} &= 1 - \left[\int_0^{\hat{\eta}} \check{f}(\hat{y} \mid \text{signal absent}) d\hat{y} \right]^{(M-1)} \\ &= 1 - \left[\gamma(\hat{\eta}, M) \right]^{(M-1)}. \end{aligned} \tag{3.30}$$

When $P_{FA} \ll 1$, it can be shown that [5]

$$P_{FA} \approx M F_c(\hat{\eta}) \tag{3.31}$$

and

$$\begin{aligned} P_D &\approx \int_{\hat{\eta}}^{\infty} \check{f}(\hat{y} \mid \text{signal present}) d\hat{y} \\ &\triangleq Q_M(\hat{\eta}, \hat{\beta}) \end{aligned} \tag{3.32}$$

where

$$\begin{aligned} F_c(\hat{\eta}) &= \int_{\hat{\eta}}^{\infty} \frac{\hat{y}^{(M-1)}}{\Gamma(M)} e^{-\hat{y}} d\hat{y} \\ &= e^{-\hat{\eta}} \sum_{n=0}^{M-1} \frac{\hat{\eta}^n}{n!} \\ &\triangleq P(M, \hat{\eta}) \end{aligned} \tag{3.33}$$

In (3.32) and (3.33), $Q_M(a, b)$ is the *Marcum's Q function of order M* and $\Gamma(\cdot)$ is the well-known *Gamma function*. $\hat{\beta}$ can be obtained from (3.19)

3.3 Computer simulation and numerical results

In this section, we present the simulation model for the acquisition schemes described in section 3.2. The performance of the detection probability P_D using the three different schemes, namely, the serial acquisition scheme, the ML acquisition scheme, and the max-threshold acquisition scheme, are investigated. The false alarm probability P_{FA} is treated as a parameter in computing the detection performance in AWGN channels.

For the serial acquisition scheme, (3.16) shows that the false alarm probability, P_{FA}, depends on P_D, P_{fa}, and P_d. By using (3.11), (3.14), and (3.15) in (3.16), P_{FA} can be computed. If we set $P_{FA} = 10^{-3}$ and that every elements in the $M \times M$ time-frequency matrix has a variance of 2, or, equivalently, the noise power equals 2, then for SNR= $-12, -11, \cdots, 0$, the corresponding threshold, η, falls in the range $(670, 677)$. We selected $\eta = 677$ in the simulation. $\eta = 695, 712, 727$ are obtained for $P_{FA} = 10^{-4}, 10^{-5}$, and 10^{-6}. Similar results can be obtained for the max-threshold acquisition scheme by using (3.31). For the moment, we assume that the noise power is perfectly known by the receiver.

3.3.1 Generation of hopping patterns

To generate a random code sequence with period M=256, a full-length shift-register cycle, also referred to as a binary Debruijn sequence[6] of length 256 is used as the PN sequence to determine the 256 carrier frequency sequence for transmission of the FH signal. A DeBruijn sequence, denoted as $\mathbf{b} = (b_0, b_1, \cdots, b_{2^n-1})$, is a periodic binary sequence with period 2^n. Every binary n-tuple, $\mathbf{b}$, occurs exactly once during one complete cycle. One advantage of the Debruijn sequence is that it has a length of power of 2. This makes the choice of the Debruijn sequence in the discrete code acquisition scheme allow efficient computation of the FFT algorithm. We set $n = 8$ so that $2^8 = 256$ unique shift-register states in one period can be generated. Algorithms for the generation of Debruijn sequence can be found in [9][10].

The frequency sequence is designed to hop between a total spectral width of W_{ss}. In the simulation, W_{ss}=1GHz, extending from DC to 1GHz. The total spectral width W_{ss} is divided by the number of the hopping tones, M, to produce M=256 hopping frequencies. The specific frequency used in a particular hop is determined by the state of the Debruijn sequence. M=256 time samples are used as the input to the FFT block and the output are M=256 discrete spectral components at 256 hopping positions.

3.3.2 Performance in AWGN

Fig. 3.9 compares the numerical performance of the serial and ML acquisition schemes. For the serial acquisition scheme, $P_D \longrightarrow 1$ as SNR $\longrightarrow -2$ dB while for the ML scheme, $P_D \longrightarrow 1$ when SNR $\longrightarrow -4$ dB. Shown in Fig. 3.10 is the numerical behavior using the max-threshold acquisition scheme whose performance is similar to that of the serial scheme.

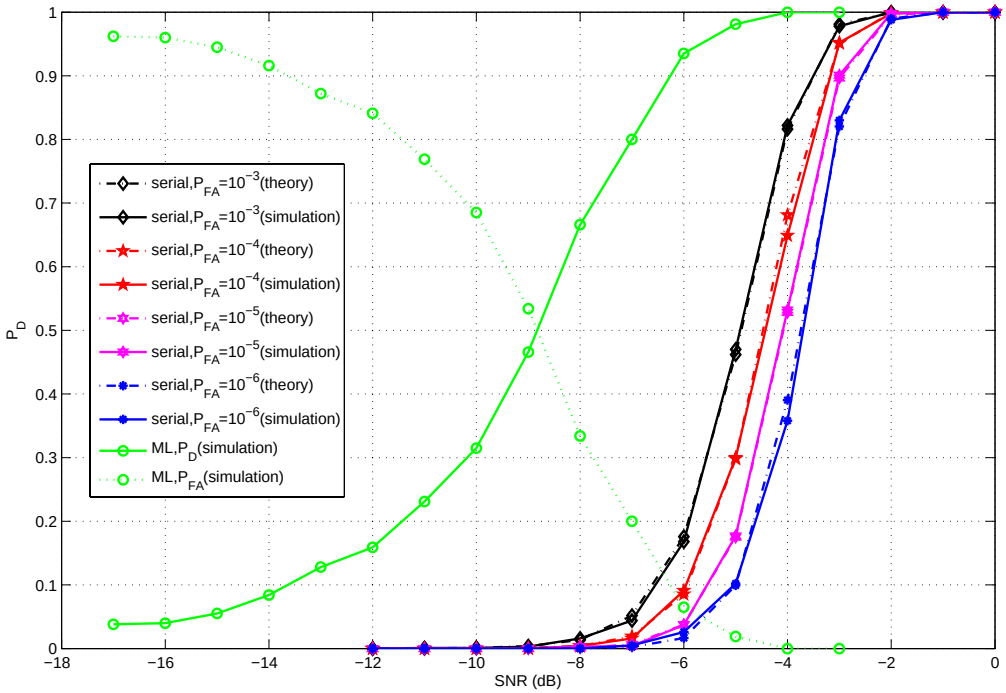

Figure 3.9: Numerical results for the serial acquisition scheme and the maximum likelihood scheme in AWGN channels;M=256.

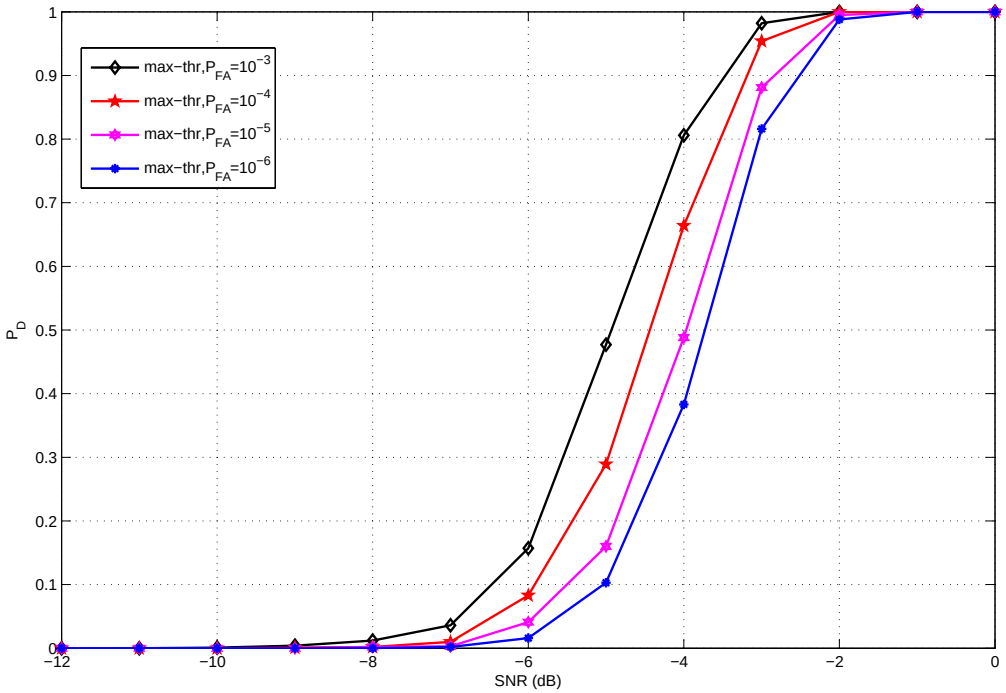

Figure 3.10: Numerical results for the max-threshold acquisition scheme in AWGN channels;M=256.

3.3.3 Impact of the hopping pattern period

All the numerical results given in the former subsection are based on a code sequence of period $M = 256$. We now examine the effect of the detection period ($M = 128$ and $M = 512$) on the detection probability performance. Fig. 3.11– 3.12 plot the performance with period $M = 128$. As expected, the performance improves as the detection period increases.

The performance of the schemes using a sync sequence of length $M = 512$ are also given in Fig. 3.13– 3.14. As expected, the performance is superior to that using a sync sequence of period $M = 256$. Although a shorter period sequence requires a faster acquisition time, it does need a higher SNR to achieve the same detection probability.

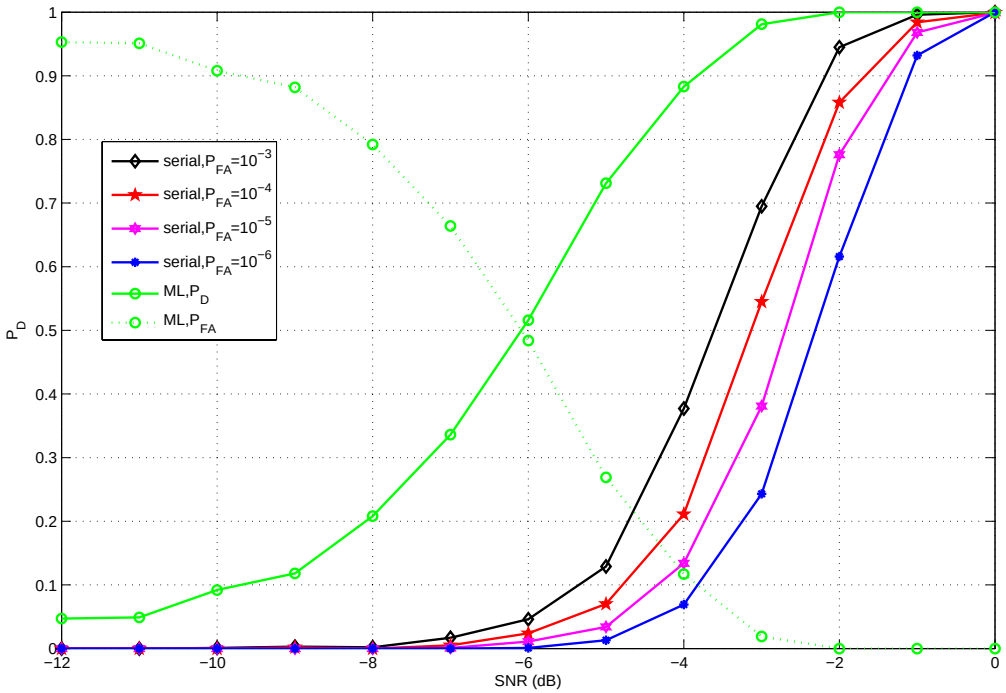

Figure 3.11: Numerical results using the serial acquisition scheme and the maximum likelihood acquisition scheme in AWGN channels; M=128.

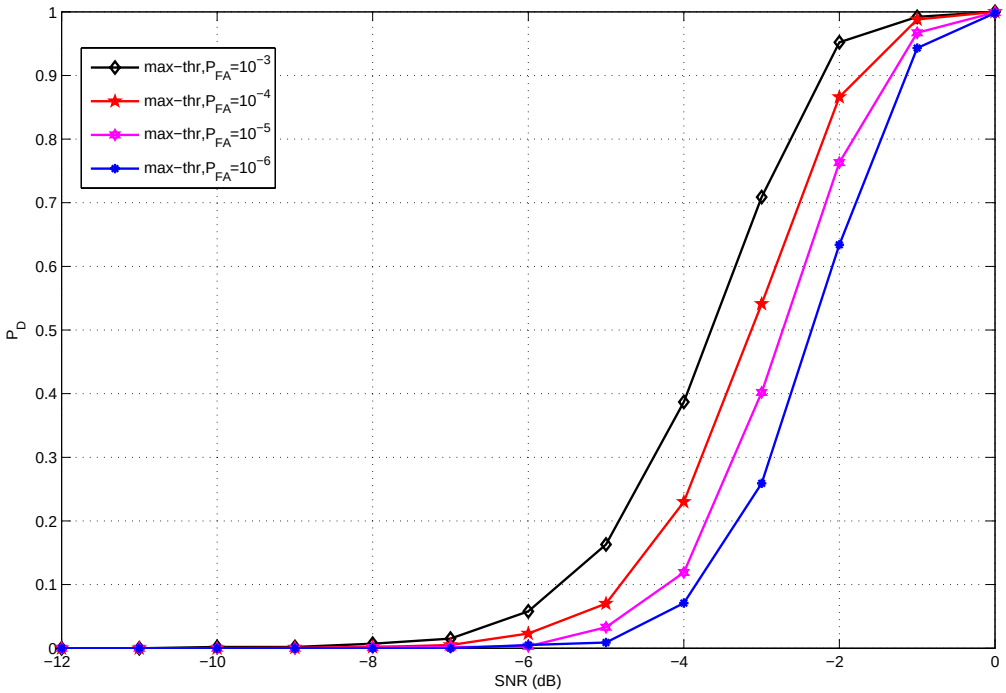

Figure 3.12: Numerical results for the max-threshold acquisition scheme in AWGN channels;M=128.

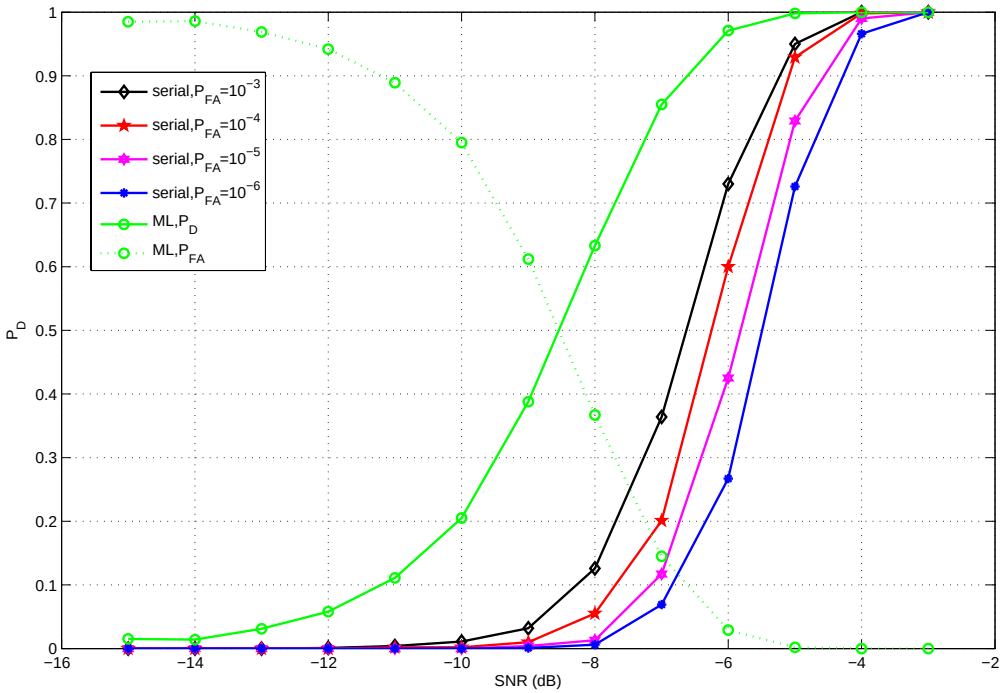

Figure 3.13: Numerical results for the serial acquisition scheme and the maximum likelihood acquisition scheme in AWGN channels;M=512.

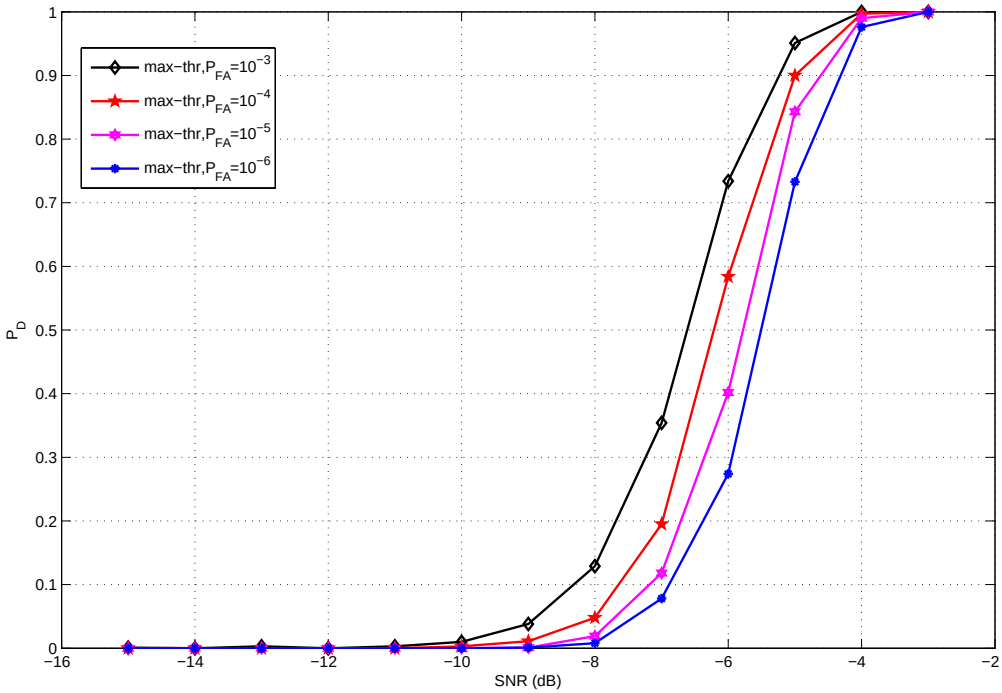

Figure 3.14: Numerical results for the max-threshold acquisition scheme in AWGN channels;M=512.

3.3.4 Mean acquisition time

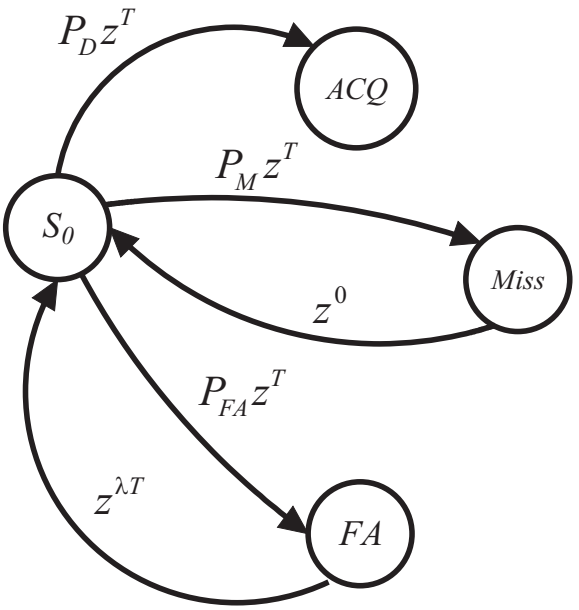

$T = MT_h$
S_0 = Start node
ACQ = Acquisition (also finish node)
$Miss$ = Miss
FA = false alarm
P_D = Detection probability
P_M = Miss probability
P_{FA} = False alarm probability
λ = Number of penalty time units due to false alarm

Figure 3.15: Transform domain state diagram for the acquisition process of the serial and the max-threshold acquisition schemes.

The acquisition time, T_{ACQ}, is defined as the time needed to acquire the correct timing. Obviously, T_{ACQ} is a random variable that depends on the acquisition scheme, the sequence period, and the operating SNR. Shown in Fig. 3.15 is the transform domain state diagram for the serial acquisition process that employs the max-threshold scheme, assuming that the acquisition process will not stop until the true hit is declared. The acquisition process always starts from the S_0 node. Following the conventions used in describing finite-state diagrams, we label each branch by the product of the transition probabilities associated with a path starting at the originating node to the terminating node of the branch. An integer (including zero) power of the variable z is used to denote the time units spent in traversing a particular branch.

The *generating function* of the acquisition time can be readily obtained from transform domain representation:

$$\begin{aligned} H(z) &= \sum_{n=1}^{\infty}\sum_{k=1}^{n} P\big(\text{ACQ after } k \text{ miss, } (n-k) \text{ false alarm}\big)\cdot z^{kT+(n-k)(\lambda+1)T+T} \\ &= \sum_{n=1}^{\infty}\sum_{k=1}^{n} P_D \cdot P_M^k \cdot P_{FA}^{(n-k)} \cdot z^{(k+1)T+(n-k)(\lambda+1)T} \end{aligned} \tag{3.34}$$

The mean acquisition time is obtained by differentiating $H(z)$ with respect to z and evaluating the result at $z = 1$

$$\begin{aligned}
\bar{T}_{ACQ} &= \frac{\partial H(z)}{\partial z}\Big|_{z=1} \\
&= \sum_{n=1}^{\infty}\sum_{k=1}^{n}\left[(k+1)T + (n-k)(\lambda+1)T\right]\cdot P_D \cdot P_M^k \cdot P_{FA}^{(n-k)} \\
&= \frac{-\lambda T P_D P_M^2 P_{FA}^{-1}}{(P_M P_{FA}^{-1}-1)(P_M-1)^2} + \frac{\lambda T P_D P_M P_{FA}^{-1}}{(P_M P_{FA}^{-1}-1)^2}\left[\frac{P_M}{1-P_M} - \frac{P_{FA}}{1-P_{FA}}\right] \\
&+ (\lambda+1)\left[\frac{P_M}{(1-P_M)^2} + \frac{P_{FA}}{(1-P_{FA})^2}\right] + \frac{P_M}{1-P_M} + \frac{P_{FA}}{1-P_{FA}} \qquad (3.35)
\end{aligned}$$

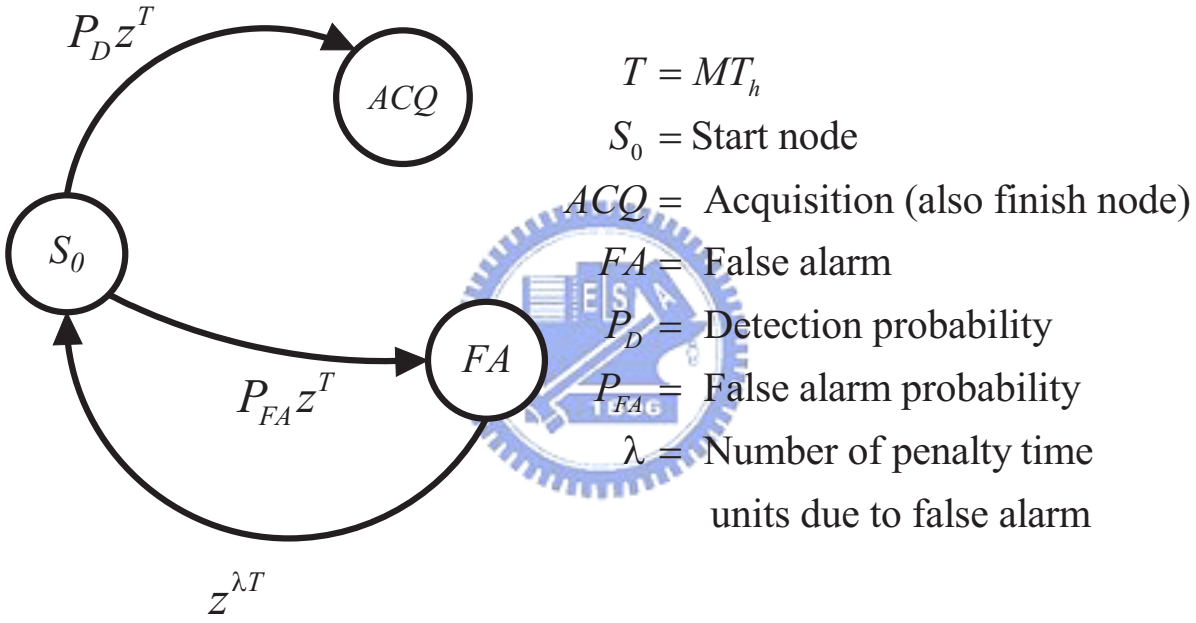

Figure 3.16: Transform domain state diagram for the acquisition process of the maximum likelihood acquisition scheme.

Fig. 3.16 shows the transform domain state diagram for the acquisition process of the ML acquisition scheme. The *generating function* of the acquisition time is

$$\begin{aligned}
H(z) &= \sum_{n=1}^{\infty} P\big(\text{ACQ after } (n-1) \text{ false alarm}\big)\cdot z^{(n-1)(T+\lambda T)+T} \\
&= \sum_{n=1}^{\infty} P_D \cdot P_{FA}^{(n-1)} \cdot z^{(n-1)(T+\lambda T)+T} \qquad (3.36)
\end{aligned}$$

The mean acquisition time is obtained by differentiating $H(z)$ with respect to z and evaluating the result at $z = 1$

$$\begin{aligned} \bar{T}_{ACQ} &= \frac{\partial H(z)}{\partial z}\Big|_{z=1} \\ &= \sum_{n=1}^{\infty} \left[(n-1)(T+\lambda T)+T\right] \cdot P_D \cdot P_{FA}^{(n-1)} \\ &= \frac{TP_D(1+\lambda P_{FA})}{(1-P_{FA})^2} \end{aligned} \tag{3.37}$$

The mean acquisition time performances of the proposed schemes are given in Fig. 3.17. It is seen that the ML acquisition scheme has a much better mean acquisition time performance than the other two.

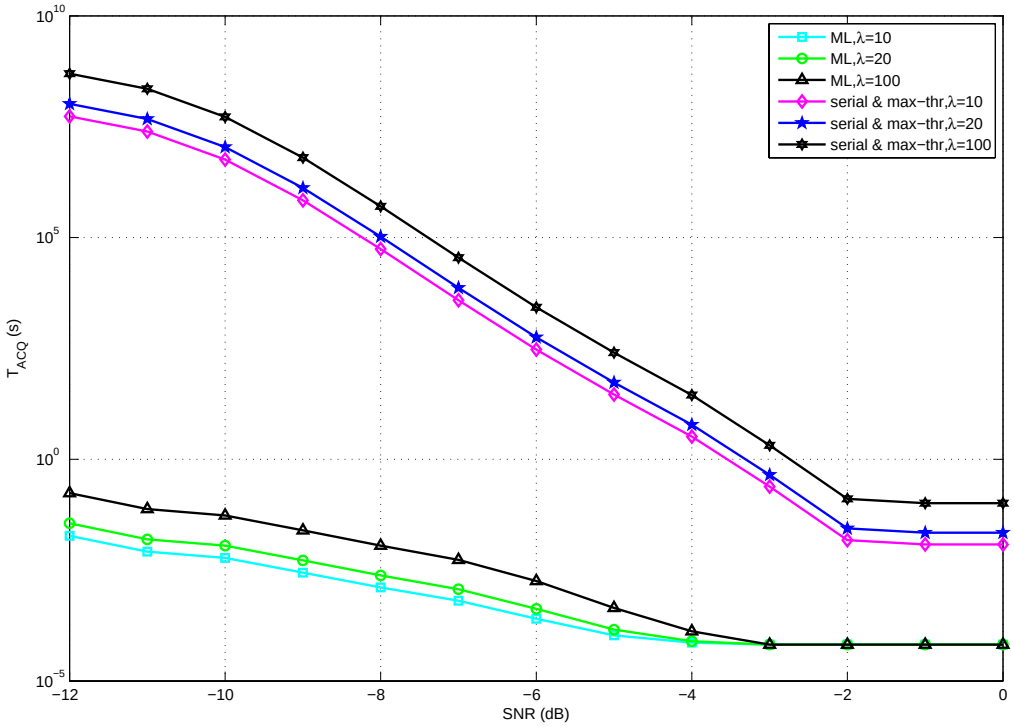

Figure 3.17: Mean acquisition time performances for various acquisition schemes.

3.4 Acquisition with imperfect noise power estimator

For the serial and the max-threshold acquisition schemes a proper threshold, η, needs to be determined so that a decision on acquisition can be made. To determine the value of η, first recall that in (3.11), $P_d = P_d(\sigma_0, \eta)$ if s is known, and from (3.14), $P_{fa} = P_{fa}(\sigma_0, \eta)$ if M is known. Using these equations in (3.15) and substituting the results in (3.16), we find that the false alarm probability can be written as a function of the standard deviation σ_0 (or equivalently, the noise power) and the threshold η.

$$P_{FA} = P_{FA}(\sigma_0, \eta) \tag{3.38}$$

Thus if σ_0 is known, or, the noise power is known, η can be determined for the required false alarm probability P_{FA}.

In the previous simulations, we assume that the $\sigma_0^2 = 1$ so that the noise power equals 2. In this way, for the serial and the max-threshold schemes with $M = 256$, $\eta = 677$ is a proper threshold for the required false alarm probability $P_{FA} = 10^{-3}$. In practical environment, we usually don't know the channel noise power in advance and have to measure or estimate it. If we want to use some particular value of η for a required false alarm probability, the incoming noise power has to be normalized to a certain value. For instance, if we use the threshold $\eta = 677$ and require a false alarm probability of 10^{-3}, the incoming noise power has to be normalized such that $\sigma_0^2 = 1$. That is to say, $\eta = 677$ is a proper threshold when $\sigma_0^2 = 1$ but not a proper one when $\sigma_0^2 \neq 1$. For the code acquisition schemes with threshold testing to function properly, the the noise power has to be estimated and normalized. Furthermore, once the received signal power is also known, together with the normalized variance, the detection probability can be predicted according to the SNR.

3.4.1 Noise power estimator using time/frequency samples

Since the DFT-based code acquisition schemes span the spectrum of the digitized version of the incoming signal plus noise, it is reasonable to perform the noise power estimation in both the frequency domain and time domain. Fig. 3.18 depicts the code acquisition scheme with noise power estimator. The outputs from the squared-magnitude DFT device are delivered to the noise power estimator. The same outputs are also sent to an accumulator which collects the squared spectral components. The noise power estimator generates the estimated noise power for each hop. The estimated noise power,

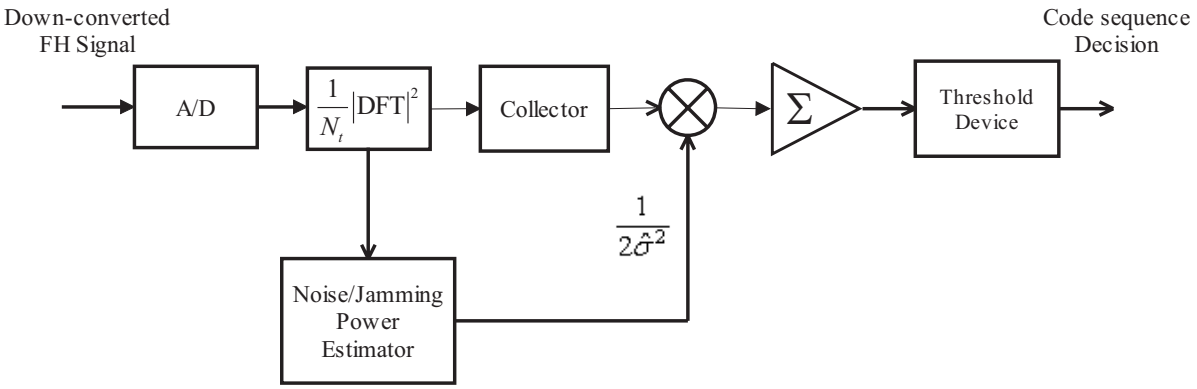

Figure 3.18: Code Acquisition Scheme with Full-band noise power estimator.

$2\hat{\sigma}^2$, is used to normalize the squared spectral components stored in the accumulator.

Fig. 3.19 illustrates the matrix of squared time-frequency elements used for power estimation. N_t is the FFT size. The $|DFT|^2$ is divided by N_t so that the power in the time domain is equal to the power in the frequency domain. Suppose that the received noise is zero-mean and has a power of $2\sigma^2$. For the first received hop interval, M squared spectral elements are generated and stored in the first column of the matrix. For the second received hop, another M squared spectral elements are generated and stored in the second column of the matrix. This process continues until the M^{th} hop is received. Thus after a single period of the code sequence, M×M squared time-frequency elements are stored in the matrix. The estimated noise power is calculated as

$$\begin{aligned} 2\hat{\sigma}^2 &= \frac{\sum_{j=1}^{M}\sum_{l=1}^{M}|z_{jl}|^2}{M \cdot N_t} \\ &= \frac{\sum_{j=1}^{M}\sum_{l=1}^{M}|z_{jl}|^2}{M^2} \end{aligned} \tag{3.39}$$

In (3.39), $N_t = M$. Note that, when the signal is absent, $|z_{jl}|^2$'s are i.i.d., central $\chi^2(2)$-distributed random variables, $\big(\chi^2(2)$ means Chi-square-distributed with degree of freedom $2\big)$, and they are non-central $\chi^2(2)$-distributed when the signal is present.

Let $\hat{\lambda} = 2\hat{\sigma}^2$ for convenience. $\hat{\lambda}$ is a sum of M^2 i.i.d., (approximately) central $\chi^2(2)$-distributed variables (when the signal is present, only M elements in the $M \times M$ matrix contain the signal components. The signal power is diminished by $10 \log M$ dB after divided by M and therefore can be ignored when it is not significantly stronger than the noise power) and therefore a (approximately) central $\chi^2(2M^2)$-distributed random variable.

$$2\hat{\sigma}^2 = \frac{\sum_{j=1}^{M}\sum_{l=1}^{M}|z_{jl}|^2}{M \cdot N_t} \tag{3.40}$$

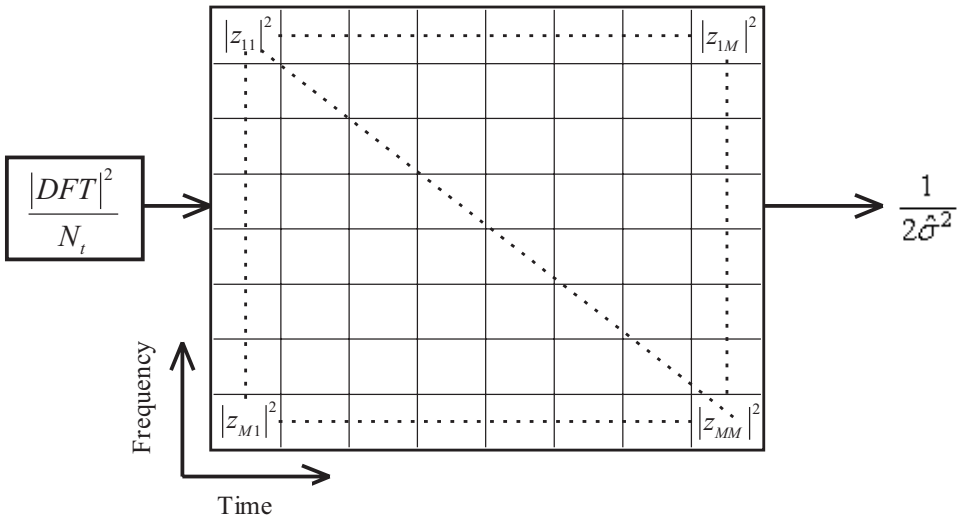

Figure 3.19: The noise/jamming power estimator performs the estimation in two dimensions, time and frequency.

The *sample mean* of $\hat{\lambda}$ is

$$\eta_{\hat{\lambda}} = \frac{1}{M^2}\sum_{j=1}^{M}\sum_{l=1}^{M}\frac{|z_{jl}|^2}{M^2} \tag{3.41}$$

The *sample variance* of $\hat{\lambda}$ is

$$\sigma_{\hat{\lambda}}^2 = \frac{1}{M^2-1}\sum_{j=1}^{M}\sum_{l=1}^{M}\left(\frac{|z_{jl}|^2}{M^2} - \eta_{\hat{\lambda}}\right)^2 \tag{3.42}$$

The PDF of $\hat{\lambda}$ can be written as

$$f_{\hat{\Lambda}}(\hat{\lambda}) = \frac{1}{2\sigma_{\hat{\lambda}}^2 \cdot \Gamma(2M^2)}\left(\frac{\hat{\lambda}}{2\sigma_{\hat{\lambda}}^2}\right)^{2M^2-1} \cdot e^{-\frac{\hat{\lambda}}{2\sigma_{\hat{\lambda}}^2}},\ \hat{\lambda} \geq 0 \tag{3.43}$$

Note that the output of the noise power estimator is the inverse of $\hat{\lambda}$.

The random variable at the input of the adder in Fig. 3.18 is a ratio of two chi-square random variables with different degree of freedom. Let's denote by $\bar{Y}_i$ the ratio $\frac{Y_i}{\hat{\lambda}}$. Since both Y_i and $\hat{\lambda}$ are non-negative, according to [13], the PDF of $\bar{Y}_i$ is

$$f_{\bar{Y}_i}(\bar{y}_i) = \int_{\hat{\lambda}=0}^{\infty} \hat{\lambda} \cdot f_{Y_i\hat{\lambda}}(\hat{\lambda}\bar{y}_i, \hat{\lambda})d\hat{\lambda} \tag{3.44}$$

If the joint PDF of Y_i and $\hat{\lambda}$, $f_{Y_i\hat{\lambda}}(\hat{\lambda}\bar{y}_i, \hat{\lambda})$ is given, $f_{\bar{Y}_i}(\bar{y}_i)$ can be computed.

The probability that a single Y_i exceeds the threshold η when the signal is present is

$$P_d = \int_{\eta}^{\infty} f_{\bar{Y}_i}(\bar{y}_i|\text{signal present})d\bar{y}_i \tag{3.45}$$

The probability that a single Y_i exceeds the threshold η when the signal is absent is

$$P_{fa} = \int_{\eta}^{\infty} f_{\bar{Y}_i}(\bar{y}_i|\text{signal absent})d\bar{y}_i \tag{3.46}$$

The detection probability P_D and the false alarm probability P_{FA} can be obtained by the same way used in the ideal cases.

3.4.2 Performance in AWGN using 2D noise power estimation

In this subsection, we give the numerical results for the aforementioned schemes with noise power estimation. For the convenience of simulation, a zero-mean AWGN process with variance (power) 2 is generated to model the channel noise. Fig. 3.20 and Fig. 3.21 illustrate the detection probability performance for various schemes when the noise power is estimated. We observe that the performance is very close to those for the ideal cases. (see Fig. 3.9 through Fig .3.10). Note that in these figures P_D for the non-ideal case is better than that for the ideal case at some points. We explain this as follows : since the normalization quantity (the estimated noise power $2\hat{\sigma}^2$) is a random variable, the random variation of $2\hat{\sigma}^2$ results in the drift of η. Recall that P_D and P_{FA} both depend on η. When η varies randomly, P_D and P_{FA} also vary randomly. Therefore, P_D for the non-ideal case can sometimes be higher than that for the ideal case.

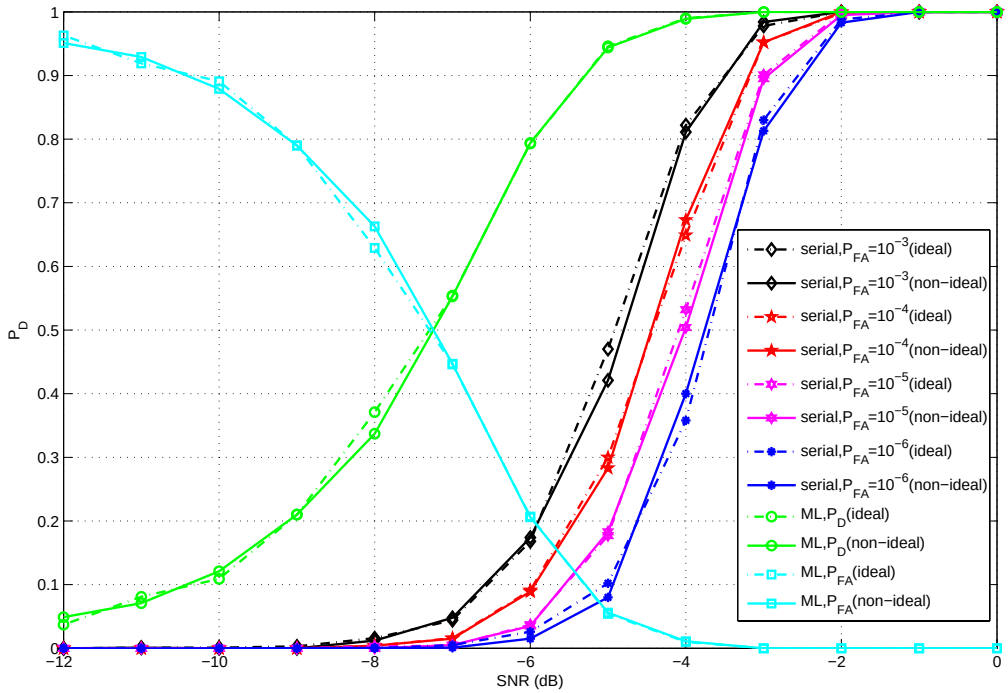

Figure 3.20: Numerical results for the serial and the ML acquisition schemes in AWGN. Both the ideal and non-ideal cases are given; M=256.

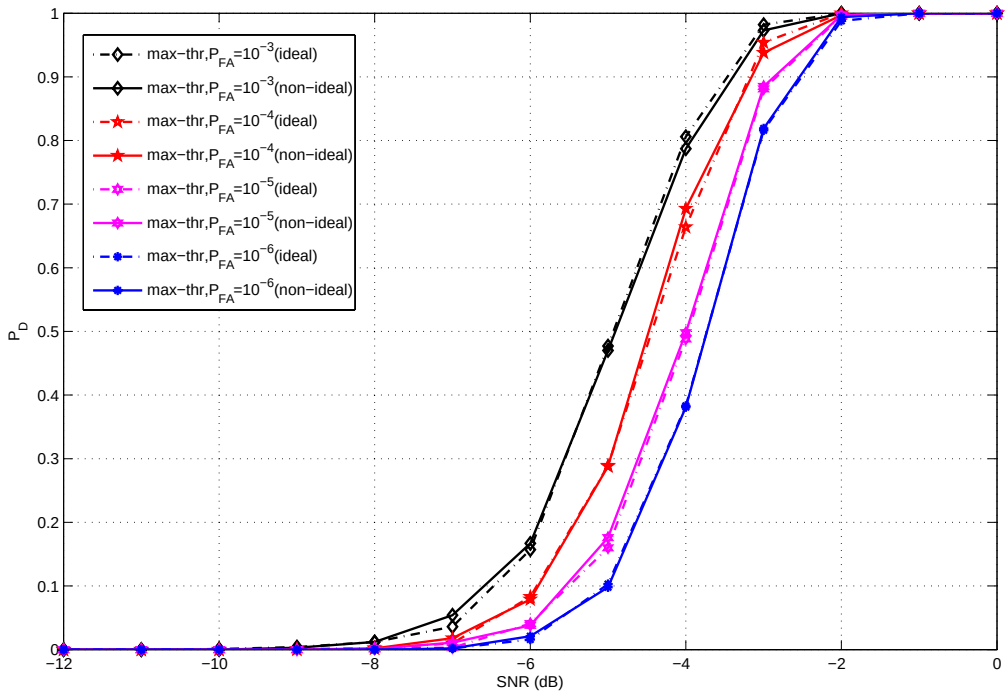

Figure 3.21: Numerical results for the max-threshold acquisition scheme in AWGN. Both the ideal and the non-ideal cases are given; M=256.

Chapter 4

Anti-Jam Performance of DFT-based Code Acquisition Schemes

In the scenario like military communication in battlefield, it is very likely that the adversary employs the communication jamming technique trying to downgrade or even disable a military communication system. When a jammer is present, both the channel AWGN noise power and the jamming power are injected into the receiver whence the performance of an acquisition scheme is degraded. To have a robust performance, a acquisition subsystem has to be capable of estimating the power of the noise and the jamming power.

In this chapter, we discuss the performances of the code (hopping pattern) acquisition schemes in a jamming environment. Two kinds of jammers, namely, the full-band noise jammer (FBNJ) and the partial-band noise jamming (PBNJ), shall be considered.

4.1 Communication jamming strategy

Two types of waveforms are often employed to jam a communication system. The first type consists of a noise signal modulated on the carrier signal. The noise has the same bandwidth with the target signal and has the effect of elevating the background noise in the jammed spectrum in which the target signal occupies. The second type also consists of a carrier signal modulated with a noise signal. The noise signal now has a bandwidth narrower than that of the target signal and thus occupies only a part of the spectrum of the target signal.

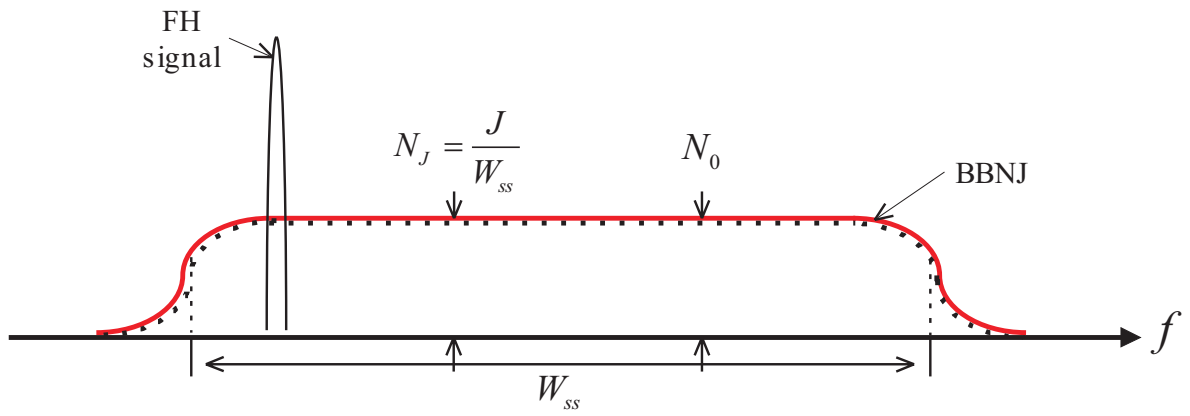

Figure 4.1: Full-band noise jamming spreading across the entire receiving spectrum.

4.2 Performance in full-band noise jamming

For the *full-band noise jamming*, a random noise waveform is modulated onto a carrier signal. The noise energy is spread across the entire spectrum used by the target receiver, as shown in Fig. 4.1. The attempt of the jammer is to interfere with the target signal by implanting the intended noise into the receiver. The FBNJ is also called *full-band jamming* or sometimes called *barrage jamming*.

Full-band noise jamming essentially brings the background noise at the receiver to a higher level, making it more difficult for the receiver to achieve successful reception from the originating transmitter. Since FBNJ increases the background noise level at the receiver, and as such, can be used to attack the code acquisition process.

The same acquisition scheme as depicted in Fig. 3.18 is used in AWGN with FBNJ. The FBNJ is modelled as an additive white Gaussian noise which is spread across the whole spectrum of the target signal. We omit the analyses since they are all the same with those performed in the AWGN cases. The numerical results are given. A 3 dB performance degradation can be seen in Fig. 4.2 and Fig. 4.3 since the FBNJ has the same power as the channel noise.

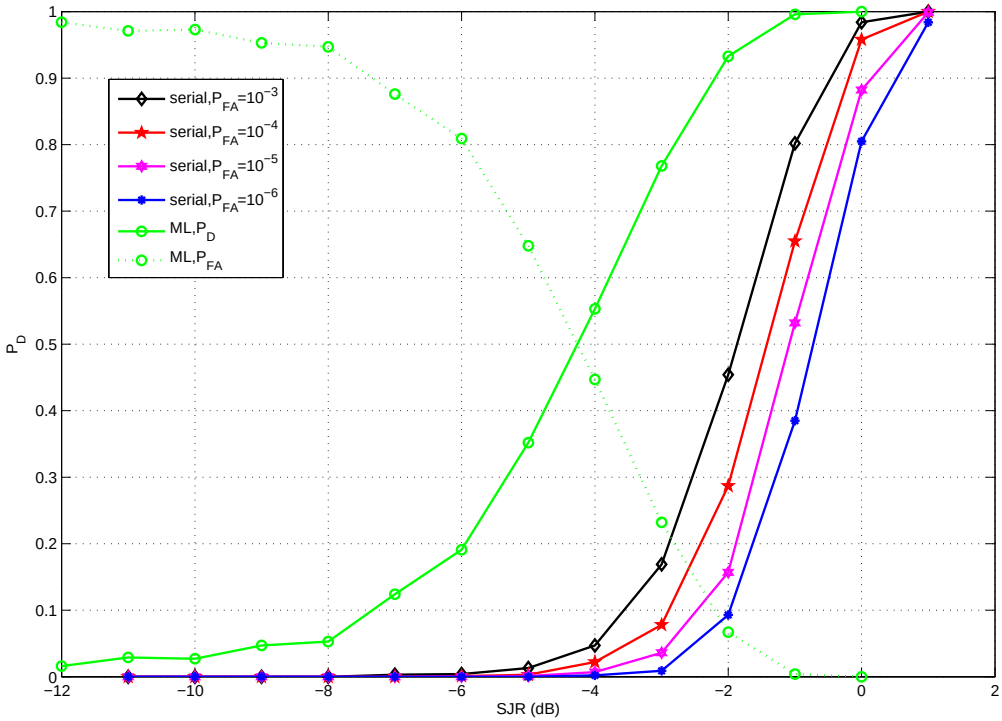

Figure 4.2: Numerical results for the serial and the ML acquisition schemes in AWGN with FBNJ;M=256.

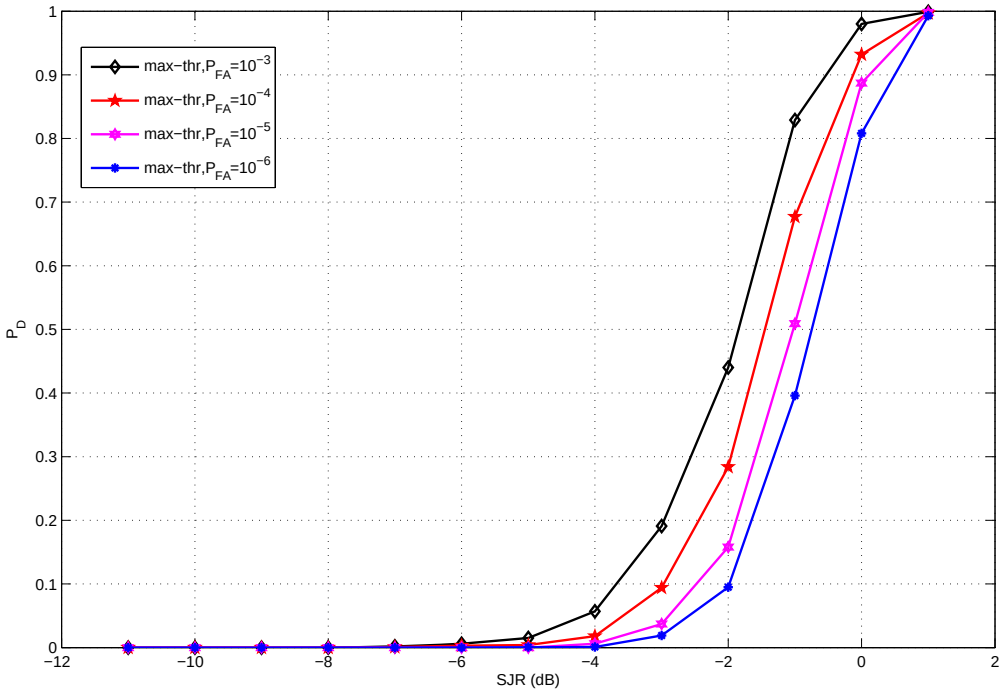

Figure 4.3: Numerical results for the max-threshold acquisition scheme in AWGN with FBNJ;M=256.

4.3 Performance in partial-band noise jamming

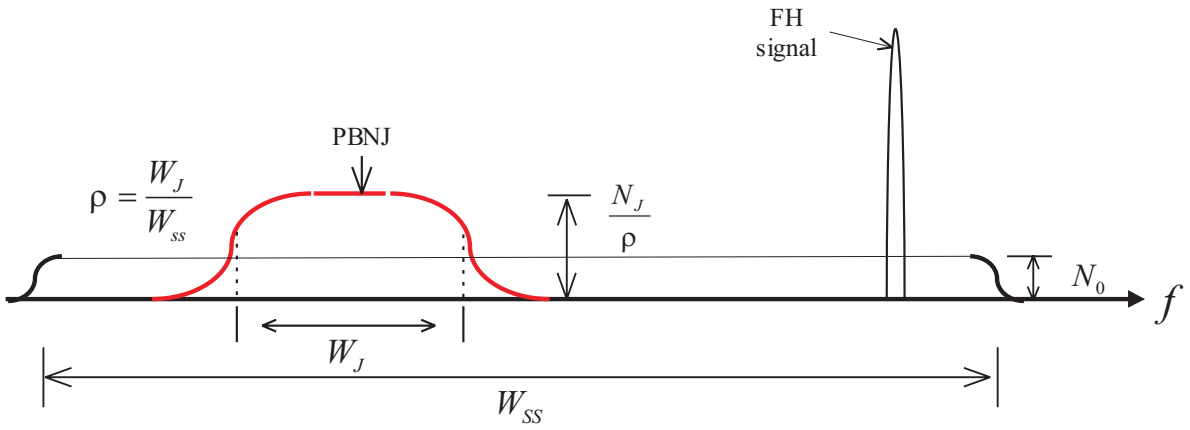

Figure 4.4: Partial-band noise jamming signal concentrates its power in a fraction of the target spectrum.

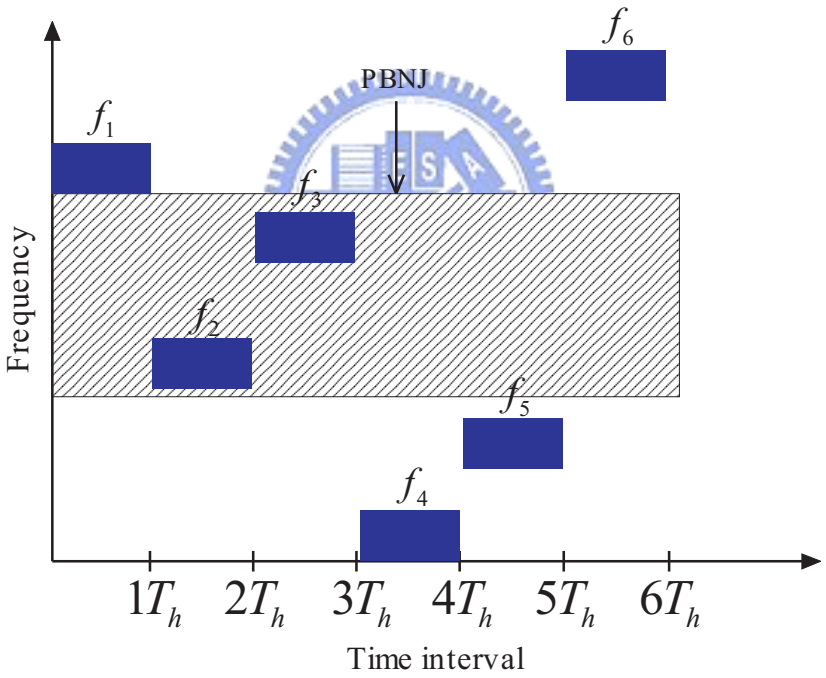

Figure 4.5: Example FH pattern in PBNJ.

Partial-band noise jamming (PBNJ) allocates and concentrates its total jamming power to a fraction of the target spectrum. The jamming power is spread across multiple channels used by the FH signal. Fig. 4.4 illustrates the PBNJ noise signal occupying a fractional part of the spectrum. Fig. 4.5 is an example FH pattern in PBNJ. Assume that the jammer is stationary, that is, it places its jamming power in some fixed channels of the FH signal. The jamming signal is modelled as an additive white Gaussian noise

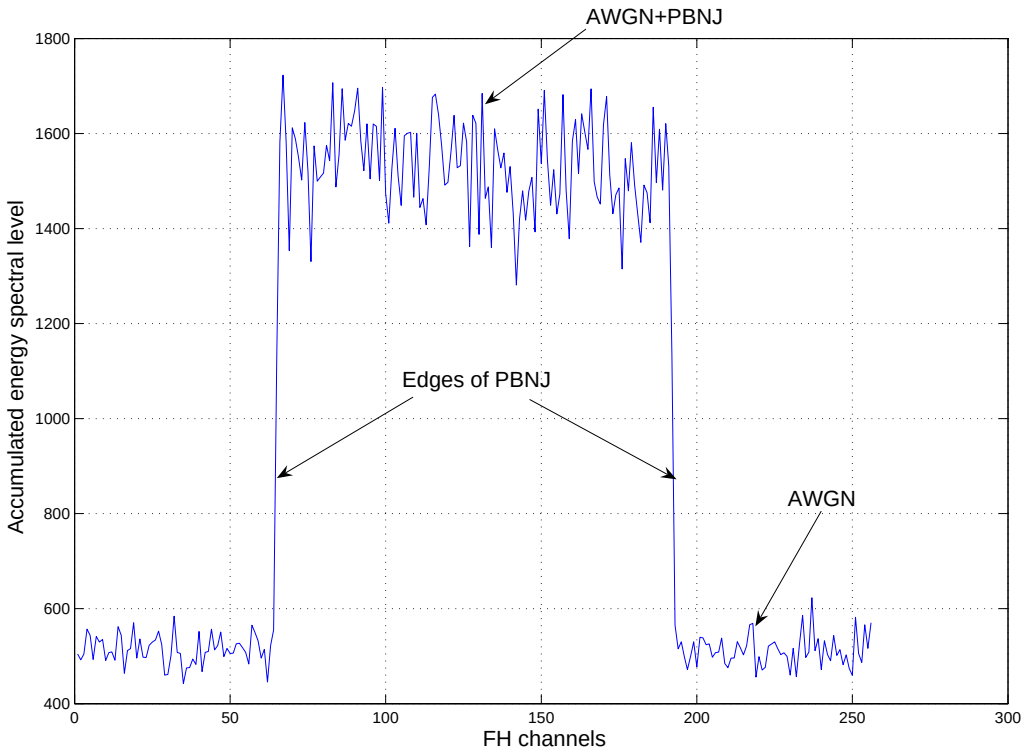

Figure 4.6: Accumulated energy spectral level in AWGN channel with PBNJ.

process with zero mean and constant power.

For the jammed channels, the noise power spectral level is

$$N_J' = N_0 + \frac{N_J}{\rho} \tag{4.1}$$

where N_0 is the power spectral level of the channel noise, N_J the power spectral level of the jamming signal if it were spread across W_{ss}, and $\rho = \frac{W_J}{W_{ss}}$ the ratio of the width of the jammed spectrum to that of the un-jammed one. The total noise power in the jammed spectrum is

$$2\sigma_J'^2 = N_J' W_J \tag{4.2}$$

For the un-jammed channels, the noise power spectral level is N_0, and the total noise power is

$$2\sigma_0^2 = N_0(W_{ss} - W_J) \tag{4.3}$$

One can see that different noise power exist in the jammed and the un-jammed spectrum from (4.2) and (4.3). Fig. 4.6 gives an example of accumulated energy spectral level, one can see that the subchannels being jammed have more accumulated energy (power)

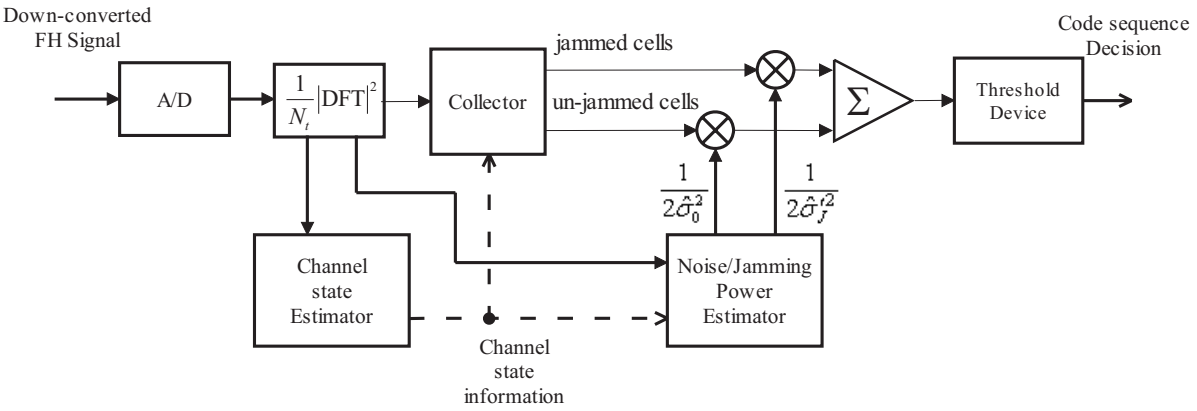

Figure 4.7: DFT-based code acquisition scheme in AWGN channel with PBNJ.

than the un-jammed ones. The net interfering power placed in the jammed subchannels is different from that in the un-jammed ones, we say that they have different channel states. For the DFT-based code acquisition schemes to function properly, the channel state information has to be acquired. This information may include how many subchannels are being jammed? Where is the edges? That is, what are the starting and ending spectral positions of the jammed spectrum? Channel state information helps the acquisition schemes in performing the channel state classification. Those channels classified as "jammed" are normalized by a quantity containing both the jamming and noise components, while the other "un-jammed" ones are normalized by another quantity containing only noise component.

To realize the channel state classification, some modifications have to be made for the code acquisition scheme in Fig. 3.18. The receiver has to know where the PBNJ noise puts its power in. Fig. 4.7 illustrates the acquisition scheme used in AWGN channel with PBNJ. The channel state estimator receives the output from the squared-magnitude DFT device and delivers the channel state information to the noise/jamming power estimator and the collector. This channel information is necessary for those two devices to distinguish the jammed subchannels from the un-jammed ones so that the power estimation and normalization process can work properly. One method used to locate the spectral edges for the PBNJ noise spectrum is to find out the maximum of the difference between any two spectral heights of two adjacent subchannels. From Fig. 4.6, one can see that the jammed subchannels has higher accumulated energy spectral level than the un-jammed subchannels. The difference between the spectral heights of the two subchannels immedi-

ately inside and outside the jammed spectrum has a maximum value among all adjacent subchannel pairs. Since there are random variations of accumulated energy resided in the PBNJ, the maximum difference can occur inside the jammed spectrum but not in the actual edges. This happens most likely especially when the accumulated jamming energy is not stronger enough than the accumulated AWGN energy in the same spectrum. One

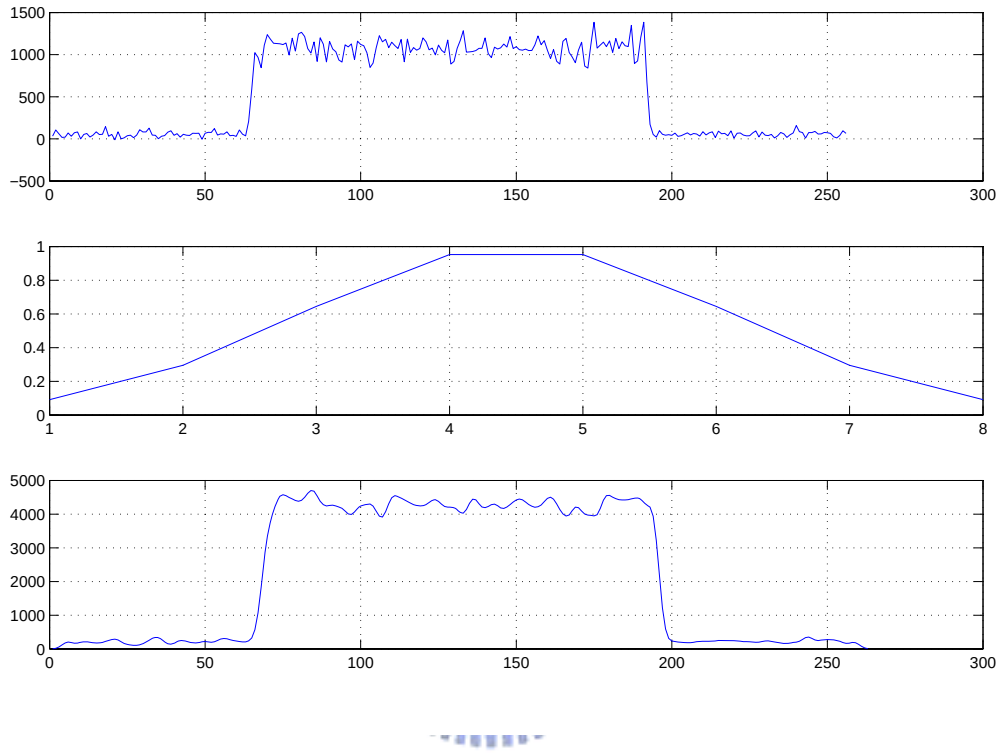

Figure 4.8: The first plot shows the accumulated power spectrum. The second plot illustrates the Gaussian window with length 8. The last plot gives the smoothed accumulated power spectrum.

way to smooth out the random variations is to convolve the spectrum with a Gaussian window before finding the maximum difference. In Fig. 4.8, one can see that the power spectrum is indeed smoothed after convolving with a Gaussian window (compare the first and the last plot). However, the smoothed PBNJ spectrum has also been broadened.

Fig. 4.9 gives the noise/power estimator in Fig. 4.7 in AWGN channel with PBNJ. In Fig. 4.9, q denotes the number subchannels being jammed per hop, $M - q$ the number of subchannels not jammed per hop. The green-shaded area represents the subchannels being jammed during one period of the code sequence. For the jammed area in the

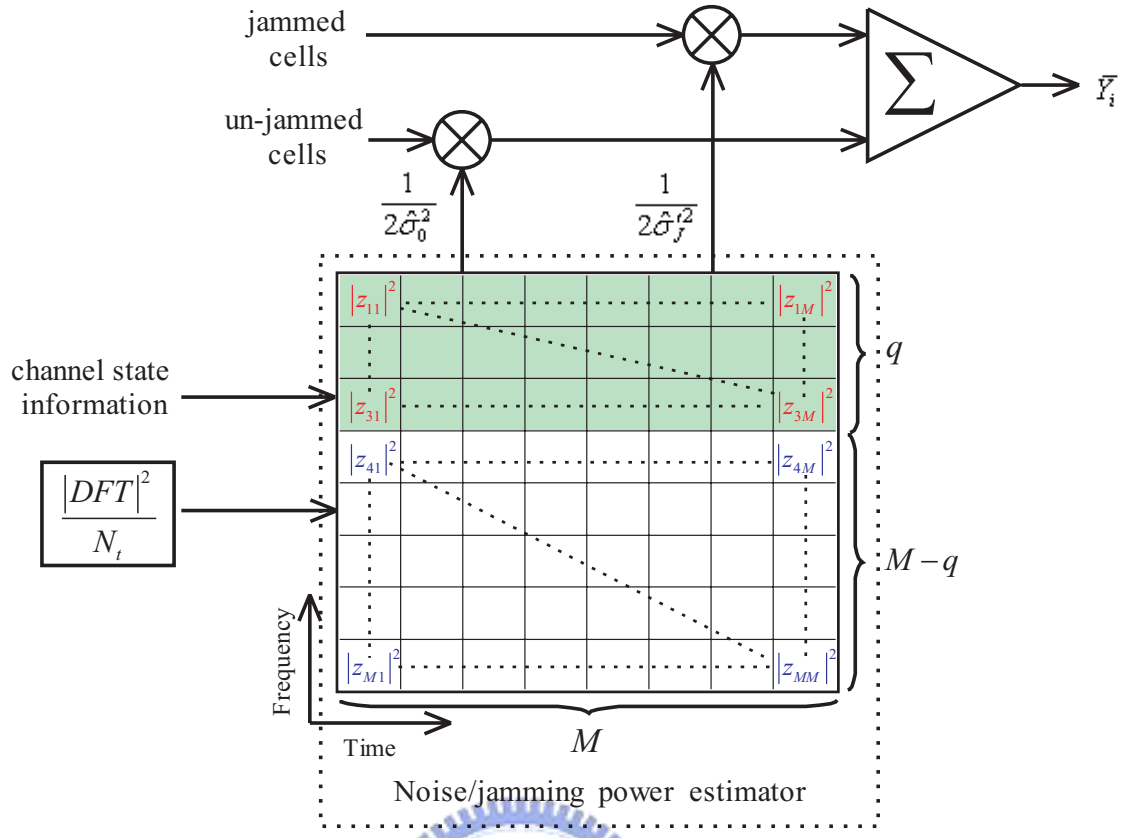

Figure 4.9: Noise/power estimator used for the acquisition scheme in Fig. 4.7.

matrix, the estimated noise power is

$$\begin{aligned} 2\hat{\sigma}\prime_J^2 &= \frac{\sum_{j=1}^{q}\sum_{l=1}^{M}|z_{jl}|^2}{M\cdot q} \\ &= \frac{\sum_{j=1}^{q}\sum_{l=1}^{M}|z_{jl}|^2}{Mq} \end{aligned} \tag{4.4}$$

For the un-jammed area in the matrix, the estimated noise power is

$$\begin{aligned} 2\hat{\sigma}_0^2 &= \frac{\sum_{j=q+1}^{M}\sum_{l=1}^{M}|z_{jl}|^2}{M\cdot(M-q)} \\ &= \frac{\sum_{j=q+1}^{M}\sum_{l=1}^{M}|z_{jl}|^2}{M(M-q)} \end{aligned} \tag{4.5}$$

Let $\hat{\varphi}=2\hat{\sigma}\prime_J^2$ and $\hat{\phi}=2\hat{\sigma}_0^2$ for convenience. For the jammed area, $|z_{jl}|^2$'s are i.i.d., (approximately) central $\chi^2(2)$-distributed random variables. The *sample mean* and *sample variance* are

$$\eta_{\hat{\varphi}}=\frac{1}{Mq}\sum_{j=1}^{q}\sum_{l=1}^{M}\frac{|z_{jl}|^2}{Mq} \tag{4.6}$$

$$\sigma_{\hat{\varphi}}^2=\frac{1}{Mq-1}\sum_{j=1}^{q}\sum_{l=1}^{M}\left(\frac{|z_{jl}|^2}{Mq}-\eta_{\hat{\varphi}}\right)^2 \tag{4.7}$$

, respectively. Its PDF is written as

$$f_{\hat{\varphi}}(\hat{\varphi}) = \frac{1}{2\sigma_{\hat{\varphi}}^2 \cdot \Gamma(2Mq)} \left(\frac{\hat{\varphi}}{2\sigma_{\hat{\varphi}}^2} \right)^{2Mq-1} \cdot e^{-\frac{\hat{\varphi}}{2\sigma_{\hat{\varphi}}^2}}, \ \hat{\varphi} \geq 0 \tag{4.8}$$

Similarly, for the un-jammed area, $|z_{jl}|^2$'s are i.i.d., (approximately) central $\chi^2(2)$-distributed random variables. The *sample mean* and *sample variance* are

$$\eta_{\hat{\phi}} = \frac{1}{M(M-q)} \sum_{j=q+1}^{M} \sum_{l=1}^{M} \frac{|z_{jl}|^2}{M(M-q)} \tag{4.9}$$

$$\sigma_{\hat{\phi}}^2 = \frac{1}{M(M-q)-1} \sum_{j=q+1}^{M} \sum_{l=1}^{M} \left(\frac{|z_{jl}|^2}{M(M-q)} - \eta_{\hat{\phi}} \right)^2 \tag{4.10}$$

, respectively. Its PDF is

$$f_{\hat{\phi}}(\hat{\phi}) = \frac{1}{2\sigma_{\hat{\phi}}^2 \cdot \Gamma\big(2M(M-q)\big)} \left(\frac{\hat{\phi}}{2\sigma_{\hat{\phi}}^2} \right)^{2M(M-q)-1} \cdot e^{-\frac{\hat{\phi}}{2\sigma_{\hat{\phi}}^2}}, \ \hat{\phi} \geq 0 \tag{4.11}$$

Let's take Fig. 4.9 as an example. The sum variable $\bar{Y}_i$ is a sum two random variables, each of which is a ratio of two chi-square random variables, that is,

$$\begin{aligned} \bar{Y}_i &= \bar{U}_i + \bar{V}_i \\ &= \frac{U_i}{\hat{\varphi}} + \frac{V_i}{\hat{\phi}}, \ i = 1, 2, \cdots, M \end{aligned} \tag{4.12}$$

where U_i is a sum of q jammed variables, i.e.,

$$\begin{aligned} U_1 &= |z_{11}|^2 + |z_{22}|^2 + \cdots + |z_{qq}|^2 \\ U_2 &= |z_{21}|^2 + |z_{32}|^2 + \cdots + |z_{1M}|^2 \\ &\vdots \\ U_M &= |z_{12}|^2 + |z_{23}|^2 + \cdots + |z_{q(q+1)}|^2 \end{aligned} \tag{4.13}$$

and V_i is a sum of $M-q$ un-jammed variables, i.e.,

$$\begin{aligned} V_1 &= |z_{(q+1)(q+1)}|^2 + |z_{(q+2)(q+2)}|^2 + \cdots + |z_{MM}|^2 \\ V_2 &= |z_{(q+1)q}|^2 + |z_{(q+2)(q+1)}|^2 + \cdots + |z_{q(q+1)}|^2 \\ &\vdots \\ V_M &= |z_{M1}|^2 + |z_{(M-1)(M)}|^2 + \cdots + |z_{(q+1)(q+2)}|^2 \end{aligned} \tag{4.14}$$

Since each $|z_{jl}|^2$ is $\chi^2(2)$-distributed, U_i is a $\chi^2(2Mq)$-distributed random variable, and V_i a $\chi^2\big(2M(M-q)\big)$-distributed random variable.

$\bar{U}_i$ is a ratio of two chi-square random variables and has a PDF

$$f_{\bar{U}_i}(\bar{u}_i) = \int_{\hat{\varphi}=0}^{\infty} \hat{\varphi} \cdot f_{U_i\hat{\varphi}}(\hat{\varphi}\bar{u}_i, \hat{\varphi}) d\hat{\varphi} \tag{4.15}$$

where $f_{U_i\hat{\varphi}}(\hat{\varphi}\bar{u}_i, \hat{\varphi})$ is the joint PDF of U_i and $\hat{\varphi}$. Similarly, $\bar{V}_i$ is also a ratio of two chi-square random variables and has a PDF

$$f_{\bar{V}_i}(\bar{v}_i) = \int_{\hat{\phi}=0}^{\infty} \hat{\phi} \cdot f_{V_i\hat{\phi}}(\hat{\phi}\bar{v}_i, \hat{\phi}) d\hat{\phi} \tag{4.16}$$

where $f_{V_i\hat{\phi}}(\hat{\phi}\bar{v}_i, \hat{\phi})$ is the joint PDF of V_i and $\hat{\phi}$.

Recall that $\bar{Y}_i$ is the sum of $\bar{U}_i$ and $\bar{V}_i$, the PDF of $\bar{Y}_i$ is the convolution of the PDF's of $\bar{U}_i$ and $\bar{V}_i$.

$$f_{\bar{Y}_i}(\bar{y}_i) = f_{\bar{U}_i}(\bar{u}_i) \otimes f_{\bar{V}_i}(\bar{v}_i) \tag{4.17}$$

where $\otimes$ denotes the convolution operation.

The probability that a single $\bar{Y}_i$ exceeds the threshold when signal present is

$$P_d = \int_{\eta}^{\infty} f_{\bar{Y}_i}(\bar{y}_i|\text{signal present}) d\bar{y}_i \tag{4.18}$$

and the probability that a single $\bar{Y}_i$ exceeds η when signal absent is

$$P_{fa} = \int_{\eta}^{\infty} f_{\bar{Y}_i}(\bar{y}_i|\text{signal absent}) d\bar{y}_i \tag{4.19}$$

The detection probability P_D and the false alarm probability P_{FA} for various acquisition schemes can then be obtained by using the same way used in the previous section.

In the numerical simulation, the method used to find the maximum difference from the raw (not smoothed) energy spectrum fails to work when $\rho = 192$ or larger is used. This is because that since the total jamming energy is fixed, the average accumulated energy level becomes lower as the total energy is spread over a wider spectrum. With the random variations residing on top of the PBNJ, it is more likely for the maximum difference to occur inside the jammed spectrum but not at the true edges. Numerical results in the AWGN channel with PBNJ are given in the following figures. Note that in these figures "raw" represents the "not smoothed" spectrum while the "smoothed" represents the "smoothed" spectrum.

Fig. 4.10 gives the numerical results in AWGN with PBNJ using the serial acquisition scheme. Fig. 4.11 and Fig. 4.12 give the numerical results in AWGN with PBNJ using the maximum likelihood acquisition scheme. Fig. 4.13 gives the numerical results in the same environment using the max-threshold acquisition scheme. It is observed that the detection probability becomes worse when ρ is getting larger at a fixed SJR point.

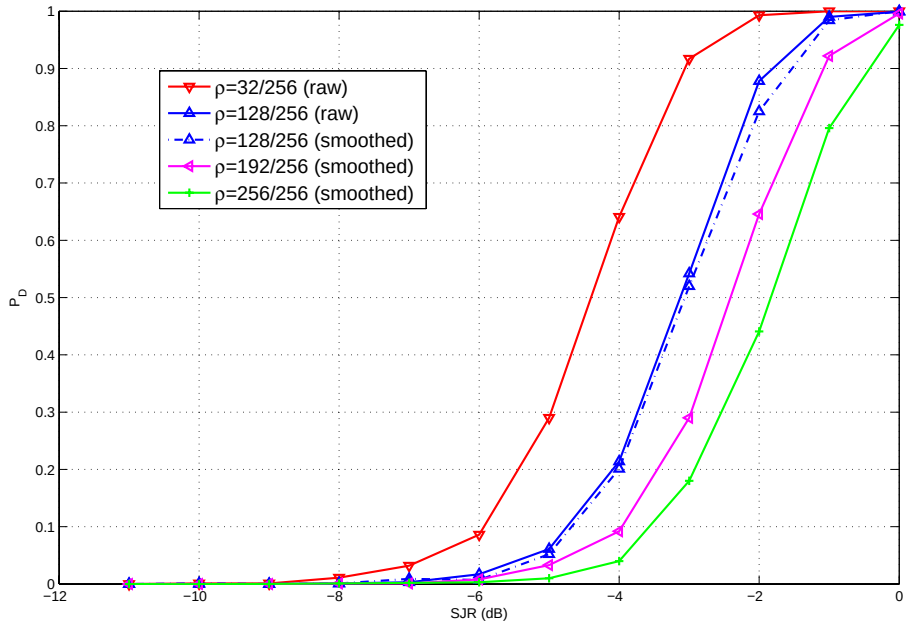

Figure 4.10: Numerical results for the serial acquisition scheme in AWGN with PBNJ. ρ represents the ratio of the number of jammed subchannels to that of the un-jammed ones;M=256.

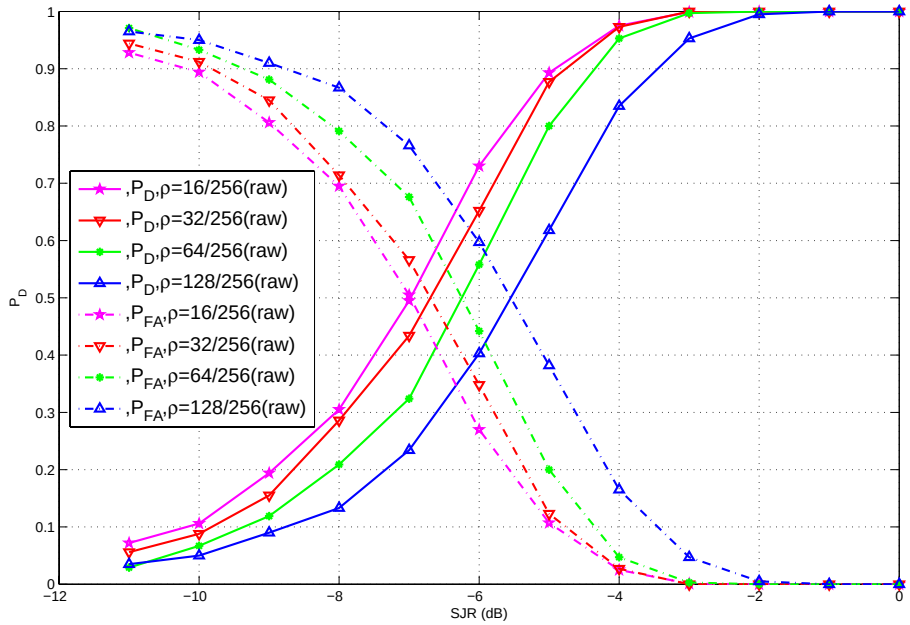

Figure 4.11: Numerical results for the maximum likelihood acquisition scheme. ρ represents the ratio of the number of jammed subchannels to that of the un-jammed ones;M=256.

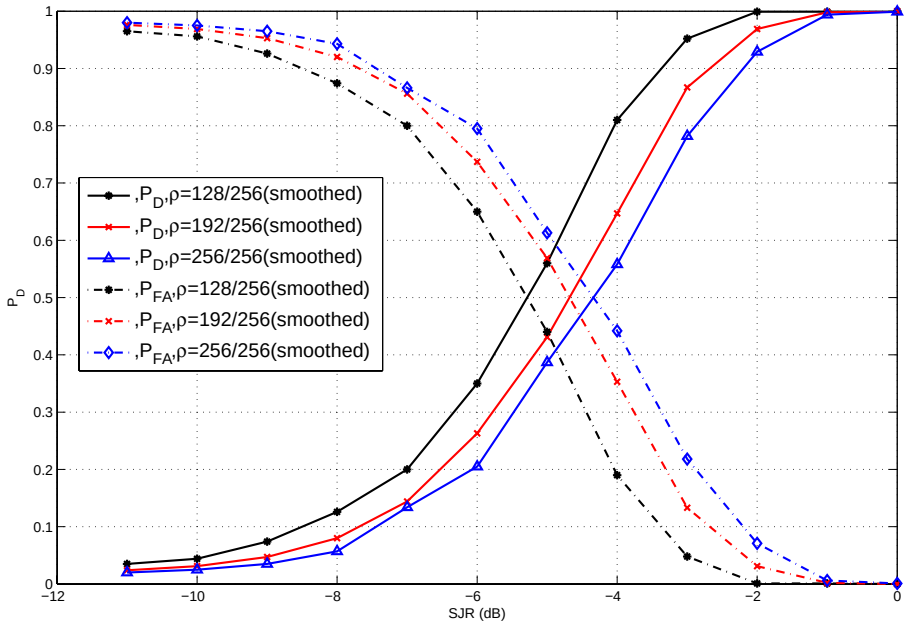

Figure 4.12: Numerical results for the maximum likelihood acquisition scheme. ρ represents the ratio of the number of jammed subchannels to that of the un-jammed ones;M=256.

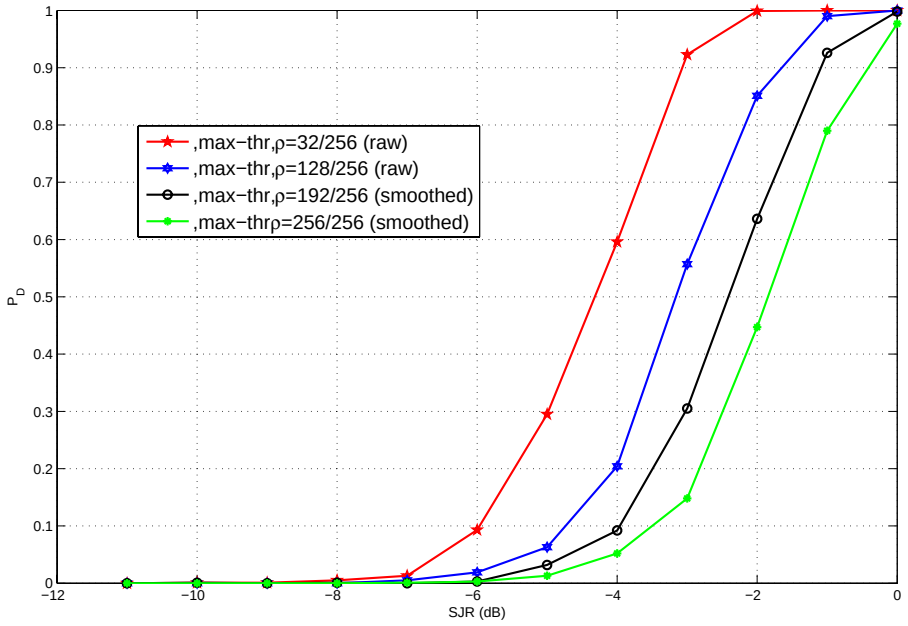

Figure 4.13: Numerical results for the max-threshold acquisition scheme in AWGN with PBNJ. ρ represents the ratio of the number of jammed subchannels to that of the un-jammed ones;M=256.

Chapter 5

Summary

In this thesis, we first briefly review some satellite communication basics and a few unique features of the earth-space satellite channel in Chapter 2. In particular, we describe the details of satellite link analysis, and consider the effect of communication jamming. Typical link budget analyses for Ka band satellite uplink communication are given. Some of these examples also studied the impact of jamming signal upon the satellite receiver and exploited the natural AJ capability of the FHSS signal.

In Chapter 3, we present a matched-filter FH code acquisition scheme and propose an equivalent DFT-based code acquisition scheme that is more efficient and can be used in an all-digital direct-conversion receiver. By virtue of the DFT operation, an efficient method that computes all possible test statistics in just one period is given. The DFT-based scheme possesses several distinct properties that the matched-filter scheme does not enjoy. Mathematical descriptions of the detection and false alarm probability for different acquisition schemes–the serial acquisition scheme, the maximum likelihood acquisition scheme, and the max-threshold acquisition scheme–in AWGN channels with perfect known noise level are derived. Numerical behaviors for these scheme are shown. The mean acquisition time versus SNR for various schemes are discussed. We find that the maximum likelihood acquisition scheme has much shorter mean acquisition time than the other two schemes although it may result in a higher false alarm probability in the same SNR. We then discuss the case that the AWGN noise power is not known and has to be estimated. In particular, we suggest a noise power estimator that uses samples in both time and spectral domains. The estimated noise power is used to normalize the squared-magnitude DFT output components. Numerical performance, including the mean acquisition time and the detection and false alarm probabilities, for the three pro-

posed acquisition schemes are also given.

In Chapter 4, two types of jammers are considered, namely, the full-band noise jammer and the partial-band noise jammer. The FBNJ introduces additional Gaussian noise so the resulting noise power level is higher than that of the AWGN. Performance analysis in FBNJ is thus identical to that of AWGN channels, except for a change of noise level. When the channel is corrupted by both AWGN and PBNJ, a channel state (CS) estimator which provides channel state information is included in the receiver. Mathematical expressions for the detection and false alarm probabilities are presented. Numerical results indicate that acceptable AJ performance is achievable. The proposed channel state estimator yields very reliable estimate so that the associated acquisition performance is close to that with ideal CS estimator.

The detection probability performance can be enhanced by increasing the EIRP of the earth station transmitter or by improving the AJ capability of the receiver. Increasing the transmit power and/or using a even higher-gain antenna can increase the EIRP. However, one have to weight the nonlinear effect associated with the high power amplifying device and the pointing error caused by a narrower beamwidth. The AJ capability can be improved by increasing the uplink spread spectrum processing gain, which can be achieved by using a hopping pattern with a longer period (which in turn requires more subchannels).

Bibliography

[1] R. M. Gagliardi, *Satellite communications*, 2nd Ed., New York, NY: Van Nostrand Reinhold, 1991.

[2] M. Richaria, *Satellite communication systems*, New York, NY:McGraw-Hilll, 1999.

[3] D. L. Adamy, *A second course in electronic warfare*, Norwood MA: Artech House Publishers, 2004.

[4] John G. Proakis, *Digital communications*, 4th Ed., New York, NY:McGraw-Hill, 2001.

[5] Y. T. Su, "Rapid code acquisition algorithms employing PN matched filters," *IEEE Trans. Commun.,* vol. 36, No. 6, pp. 724-733, June 1988.

[6] N. G. de Bruijn, "A combinatorial problem," *Nederl. Akad. Wetensch. Proc.*, vol. 49, pp. 758-754, June 1946.

[7] C.-D. Chung and P.-C. Huang, "Effects of fading and partial-band noise jamming on a fast FH/BFSK acquisition receiver with noise-normalization combination," *IEEE Trans. Commun.,* vol. 44, No. 1, Jan. 1996.

[8] Wern-Ho Sheen, Chun-Chieh Tseng, and Huan-Chun Wang, "Multiple-dwell and sequential code acquisition with diversity for FFH/MFSK spread-spectrum system under band multitone jamming," *IEEE Trans. Commun.,* vol. 48, No. 5, May 2000.

[9] T. Etzion, and A. Lempel, "Algorithms for the generation of full-length shift register sequence," *IEEE Trans. Inform. Theory,* vol. IT-30, No. 3, pp. 480-484, May 1984.

[10] C. J. A. Jansen, W. G. Franx, and D. E. Boekee, "An efficient algorithm for the generation of DeBruijn cycles", *IEEE Trans. Inform. Theory,* vol. 37, No. 5, pp. 1475-1478, Sep. 1991.

[11] M. K. Simon, J. K. Omura, R. A. Scholtz, and B. K. Levitt, *Spread spectrum communications handmook*, Part II, Ch.2, NY:McGraw-Hill, 2002.

[12] D. J. Torrieri, *Principles of secure communication systems*, Norwood MA:Artech House, 1992.

[13] A. Papoulis, and S. U. Pillai, *Probability, Random variables and stochastic processes*, 4th ed., New York, NY:McGraw-Hill, 2002.

[14] A. V. Oppenheim and R. W. Schafer, *Discrete-time Signal Processing*, 2nd ed., Upper Saddle River, NJ:Prentice-Hall, 1999.

作 者 簡 歷

張祖瑞

男，1974 年出生於台灣花蓮

民國八十一年畢業於省立花蓮高中

民國八十五年畢業於中正理工學院電機工程學系

民國九十年進入國立交通大學電機資訊學院，九十三年起師蘇育德教授，從事無線通訊系統方面研究，從中獲益良多。

民國九十六年一月獲得電信工程碩士學位。

Graduate Courses：

1. 數位訊號處理
2. 類比積體電路
3. 天線與電波傳播
4. 個人通訊
5. 微波工程
6. 隨機過程
7. 計算機網路
8. 數位通訊